

FINAL TECHNICAL REPORT

FOR NASA GRANT NAG-3-577

Entitled


FLUID PHYSICS PHENOMENA OF RESISTOJET THRUSTERS

Prepared for

NASA Lewis Research Center  
Cleveland, Ohio 44135

by

Principal Investigator:

  
Kenneth J. De Witt  
Distinguished University Professor  
Department of Chemical Engineering  
The University of Toledo  
Toledo, Ohio 43606

Submitted JUNE, 1996  
for the expiration date of  
12-31-95

FINAL REPORT for NAG 3-577

The work done under this grant from NASA Lewis was completed in December, 1995. The grant was used to support the research performed by K. J. De Witt and T. G. Keith, Jr., of the University of Toledo and their graduate students. The majority of the work was performed on-site at the NASA Lewis Research Center in Cleveland, Ohio.

The attached sheet of publications, along with part of an M.S. thesis by Tony Howell, constitutes the final report for this grant. All of these publications are available in the open literature, and all have previously been submitted to the grant technical monitor.

RESEARCH PUBLICATIONS FROM NASA GRANT NAG 3-577

- [1] Howell, T. G., "Analyses in Theoretical and Experimental Fluid Flow", M.S. Thesis, The University of Toledo, Toledo, Ohio, 1995.
- [2] Chung, C. H., K. J. De Witt, R. M. Stubbs and P. F. Penko, "Simulation of Overexpanded Low-Density Nozzle Plume Flow", AIAA Journal 33, 1646-1650, No. 9, Sept., 1995.
- [3] Chung, C. H., S. C. Kim, R. M. Stubbs and K. J. De Witt, "Low Density Nozzle Flow by the Direct Simulation Monte Carlo and Continuum Methods", J. Propulsion and Power 11, No. 1, 64-70, Jan.-Feb., 1995.
- [4] Chung, C. H., S. C. Kim, K. J. De Witt and H. T. Nagamatsu, "Numerical Analysis of Hypersonic Low-Density Scramjet Inlet Flow", J. Spacecraft and Rockets 32, No. 1, 60-66, Jan.-Feb., 1995.
- [5] Chung, C. H., K. J. De Witt, D. R. Jeng and T. G. Keith, Jr, "Numerical Analysis of Rarefied Gas Flow Through Two-Dimensional Nozzles", J. Propulsion and Power 11, No. 1, 71-78, Jan.-Feb., 1995.
- [6] Chung, C. H., K. J. De Witt and D. R. Jeng, "Direct Simulation Monte Carlo Analysis of Detailed Flow Structures in Gas Mixtures, "Rarefied Gas Dynamics: Theory and Simulations, edited by B. D. Shizgal and D. P. Weaver, Vol. 159, Progress in Astronautics and Aeronautics, AIAA, Washington, D.C., 1994, 243-255.
- [7] Penko, P. F., I. D. Boyd, D. L. Meissner and K. J. De Witt, "Measurement and Analysis of a Small Nozzle Plume in Vacuum," J. Propulsion and Power 9, No. 4, 646-648, 1993.
- [8] Meissner, D. L., "Experimentation in the Low-Density Plume of a Simulated Electrothermal Thruster for Computer Code Validation, NASA C.R. 191112, April, 1993.
- [9] Chung, C. H., K. J. De Witt, D. R. Jeng and P. F. Penko, "Internal Structure of Shock Waves in Disparate Mass Mixtures," J. Thermophysics and Heat Transfer 7, No. 4, 742-744, 1993.
- [10] Chung, C. H., K. J. De Witt, S. C. Kim and R. M. Stubbs, "DSMC and Continuum Analysis of Low-Density Nozzle Flow", Paper No. AIAA-93-0727, Presented at the AIAA 31st Aerospace Sciences Meeting, Reno, Nevada, January, 1993.
- [11] Chung, C. H., K. J. De Witt, S. C. Kim and R. M. Stubbs, "Analysis of Plume Backflow Around a Nozzle Lip in a Nuclear Rocket", Paper No. AIAA-93-2497, Presented at the

29th Joint Propulsion Conference, Monterey, California,  
June, 1993.

- [12] Chung, C. H., K. J. De Witt, S. C. Kim and H. Nagamatsu,  
"DSMC Analysis of Hypersonic Low Density Flows Around a  
Scramjet Inlet", Paper No. AIAA-93-2870, Presented at the  
28th Thermophysics Conference, Orlando, Florida, July,  
1993.
- [13] Meissner, D. L., "Theoretical and Experimental  
Investigations of Fluid and Thermal Physics," M.S. Thesis,  
University of Toledo, 1992, directed by D. R. Jeng, P. F.  
Penko, K. J. De Witt and T. G. Keith, Jr.
- [14] Boyd, I. D., P. F. Penko, D. L. Meissner and K. J. De Witt,  
"Experimental and Numerical Investigations of Low-Density  
Nozzle and Plume Flows of Nitrogen," AIAA Journal 30, No.  
10, 2453-2461, October, 1992.
- [15] Penko, P. F., I. D. Boyd, D. L. Meissner and K. J. De Witt,  
"Measurement and Analysis of a Small Nozzle Plume in  
Vacuum," Paper No. AIAA 92-3108, Presented at the AIAA  
28th Joint Propulsion Conference, Nashville, Tennessee,  
July, 1992.
- [16] Chung, C. H., K. J. De Witt, D. R. Jeng and T. G.  
Keith, Jr., "Numerical Simulation of Rarefied Flow Through  
A Slit," J. Thermophysics and Heat Transfer 6, No. 1, 27-  
34, January, 1992.
- [17] Chung, C. H., K. J. De Witt, D. R. Jeng and P. F. Penko,  
"FDDO and DSMC Analyses of Rarefied Gas Flow Through 2D  
Nozzles", Paper No. AIAA-92-2858, Presented at the AIAA  
28th Joint Propulsion Conference, Nashville, Tennessee,  
July, 1992.
- [18] Chung, C. H., K. J. De Witt, D. R. Jeng and P. F. Penko,  
"DSMC Analysis of Species Separation in Rarefied Gas  
Flows", Paper No. AIAA-92-2859, Presented at the AIAA  
28th Joint Propulsion Conference, Nashville, Tennessee,  
July, 1992.
- [19] Flowe, A. C., K. J. De Witt, T. G. Keith, Jr., G. E. Pawlas  
and P. F. Penko, "Numerical Modeling of Fluid and  
Electromagnetic Phenomena in an Arcjet," Paper No. AIAA-  
92-3106, Presented at the AIAA 28th Joint Propulsion  
Conference, Nashville, Tennessee, July, 1992.
- [20] Chung, C. H., K. J. De Witt, D. R. Jeng and T. G.  
Keith, Jr., "Numerical Simulation of Rarefied Flow Through  
A Slit," J. Thermophysics and Heat Transfer 6, No. 1, 27-  
35, Jan.-March, 1992.

- [21] Manzella, D. H., P. F. Penko, K. J. De Witt and T. G. Keith, Jr., "Test-Cell Pressure Effects on the Performance of Resistojets", J. Propulsion and Power 7, 269-274, 1991.
- [22] Chung, C. H., K. J. De Witt and D. R. Jeng, "New Approach in Direct-Simulation of Gas Mixtures," Paper No. AIAA-91-1343, Presented at the AIAA 26th Thermophysics Conference, Honolulu, Hawaii, June, 1991.
- [23] Manzella, D. H., P. F. Penko, K. J. De Witt and T. G. Keith, Jr., "The Effect of Ambient Pressure on the Performance of a Resistojet," J. Propulsion and Power 5, 452-456, 1989.
- [24] Manzella, D. H., P. F. Penko, K. J. De Witt and T. G. Keith, Jr., "An Experimental Investigation of the Effect of Test-Cell Pressure on the Performance of Resistojets", 24th AIAA/ASME/SAE/ASEE Joint Propulsion Conference, Paper No. AIAA-88-3286, July, 1988.
- [25] Manzella, D. H., "An Experimental Investigation of the Effect of Cell Pressure on the Performance of Resistojets", M.S. Thesis, The University of Toledo, Toledo, Ohio, 1987.
- [26] Manzella, D. H., P. F. Penko, K. J. De Witt and T. G. Keith, Jr., "The Effect of Ambient Pressure on the Performance of a Resistojet", 19th AIAA/DLGR/JSASS International Electric Propulsion Conference, Paper No. AIAA 87-0991, May, 1987.

A Thesis

entitled

**ANALYSES IN THEORETICAL AND EXPERIMENTAL FLUID FLOW**

by

Tony G. Howell

as partial fulfillment of the requirements of

the Master of Science Degree in

Chemical Engineering

---

Co-Advisor

---

Co-Advisor

---

Graduate School

The University of Toledo

March, 1996

## ACKNOWLEDGMENTS

I would like to thank my advisors, Dr. Kenneth J. DeWitt and Dr. Duen-Ren Jeng, for their constant guidance and support throughout my research endeavor. I would also like to thank Dr. Paul F. Penko for being coadvisor for my work at NASA Lewis, and Dr. Theo G. Keith, Jr., for serving on my final examination committee. I also wish to thank Dr. Michael R. Cameron for his generous assistance in helping debug the computer codes.

It is with sincere appreciation that I thank the NASA Lewis Research Center for their financial assistance under grant NAG 3-577 during my graduate work. Finally, I wish to thank my wife, Kelly, and my parents for without them and their reassuring words, this research could not have been possible. I dedicate my thesis to them.

Tony Gilbert Howell

March 1996

## TABLE OF CONTENTS

ACKNOWLEDGMENTS .....	ii
TABLE OF CONTENTS .....	iii
LIST OF TABLES .....	vi
LIST OF FIGURES .....	viii
NOMENCLATURE .....	x
ABSTRACT .....	xiii

**Part I:        A Theoretical and Numerical Analysis of Momentum and  
Heat Transfer in the Laminar Boundary Layer of a  
Continuously Stretching Two-Dimensional Solid Surface  
Moving in a Semi-Infinite, Quiescent Power-Law Fluid**

<b>CHAPTER I        Introduction .....</b>	<b>2</b>
1.1    Literature Review .....	2
1.2    Classification of Fluids .....	4
1.3    Goals of This Study .....	5
<b>CHAPTER II       Formulation of Momentum Boundary Layer Equations .....</b>	<b>7</b>
2.1    General Assumptions and Problem Description .....	7
2.2    Governing Momentum Boundary Layer Equations .....	8
2.3    Coordinate Transformation .....	8
2.4    Series Solution .....	11
<b>CHAPTER III      Numerical Analysis of <math>f_i</math> Equations .....</b>	<b>14</b>
3.1    Integration Technique .....	16
3.2    Tabulation of Significant Wall Derivatives .....	18



3.3	Important Momentum Boundary Layer Quantities .....	24
3.3.1	Local Friction Coefficient .....	24
3.3.2	Boundary Layer Thicknesses .....	24
<b>CHAPTER IV</b>	<b>Formulation of Thermal Boundary Layer Equations ..</b>	<b>30</b>
4.1	Description of Problem and Assumptions .....	30
4.2	Governing Thermal Boundary Layer Equations .....	31
4.3	Coordinate Transformation .....	32
4.4	Series Solution .....	34
<b>CHAPTER V</b>	<b>Numerical Analysis of <math>\theta_i</math> Equations .....</b>	<b>38</b>
5.1	Closed Form Solution of $\theta_0$ .....	38
5.2	Numerical Solutions of $\theta_1$ , $\theta_2$ , and $\theta_3$ .....	38
5.3	Tabulation of Universal Temperature Functions .....	40
5.4	Important Thermal Boundary Layer Quantities .....	47
5.4.1	Surface Heat Flux .....	47
5.4.2	Nusselt Number .....	47
5.5	Applications .....	48
5.5.1	Non-Linear Surface Velocity for Stretched Surface .....	48
5.5.2	Linear Surface Velocity for Stretched Surface .....	49
<b>CHAPTER VI</b>	<b>Conclusions .....</b>	<b>52</b>
<b>REFERENCES</b>	<b>.....</b>	<b>54</b>
<b>APPENDIX A</b>	<b>Code Listings .....</b>	<b>56</b>

**Part II:      An Experimental Analysis of Low-Density Plume Flow Angles  
and Impingement for Code Validation**

<b>CHAPTER I</b>	<b>Introduction</b>	<b>85</b>
1.1	Introduction to Electrothermal Thrusters	85
1.2	Previous Experimental and Numerical Studies	85
1.3	Contents of this Study	87
<b>CHAPTER II</b>	<b>Experimental Apparatus, Procedure, and Uncertainty</b>	<b>88</b>
2.1	Experimental Apparatus	88
2.2	Experimental Procedure	93
2.3	Uncertainty	95
2.3.1	Local Flow Angle	96
2.3.2	Impingement Pressures	97
<b>CHAPTER III</b>	<b>Experimental Results and Discussion</b>	<b>99</b>
3.1	Run Definitions	99
3.2	Experimental Results	103
3.2.1	Argon Local Flow Angles	103
3.2.2	Nitrogen Plume Impingement Pressures	106
3.3	Direct-Simulation Monte Carlo Results	109
3.4	Discussion	115
<b>CHAPTER IV</b>	<b>Conclusions and Recommendations</b>	<b>118</b>
<b>REFERENCES</b>		<b>120</b>

## LIST OF TABLES

### **Part I**

Table 3.1:	Convergence criteria and numerical settings for computer codes .	18
Table 3.2:	Numerical results of $f''(0)$ for $n = 1.0$ with those of Jeng et al. [21] .....	20
Table 3.3:	Numerical results for $f''(0)$ for $n = 0.3$ .....	21
Table 3.4:	Numerical results for $f''(0)$ for $n = 0.5$ .....	21
Table 3.5:	Numerical results for $f''(0)$ for $n = 0.7$ .....	21
Table 3.6:	Numerical results for $f''(0)$ for $n = 0.9$ .....	22
Table 3.7:	Numerical results for $f''(0)$ for $n = 1.1$ .....	22
Table 3.8:	Numerical results for $f''(0)$ for $n = 1.3$ .....	22
Table 3.9:	Numerical results for $f''(0)$ for $n = 1.5$ .....	23
Table 3.10:	Numerical results for $f''(0)$ for $n = 1.7$ .....	23
Table 3.11:	Numerical results for $f''(0)$ for $n = 1.9$ .....	23
Table 3.12:	Functions related to displacement thickness for $n = 1.0$ with those of Jeng et al. [21] .....	26
Table 3.13:	Functions related to displacement thickness for $n = 0.3$ .....	27
Table 3.14:	Functions related to displacement thickness for $n = 0.5$ .....	27
Table 3.15:	Functions related to displacement thickness for $n = 0.7$ .....	27
Table 3.16:	Functions related to displacement thickness for $n = 0.9$ .....	28
Table 3.17:	Functions related to displacement thickness for $n = 1.1$ .....	28
Table 3.18:	Functions related to displacement thickness for $n = 1.3$ .....	28
Table 3.19:	Functions related to displacement thickness for $n = 1.5$ .....	29
Table 3.20:	Functions related to displacement thickness for $n = 1.7$ .....	29
Table 3.21:	Functions related to displacement thickness for $n = 1.9$ .....	29

Table 5.1:	Results for universal functions for a step-change in temperature .	41
Table 5.2:	Results for universal functions for a step-change in temperature .	42
Table 5.3:	Results for universal functions for a step-change in temperature .	43
Table 5.4:	Results for universal functions for a step-change in temperature .	44
Table 5.5:	Results for universal functions for a step-change in temperature .	45
Table 5.6:	Results for universal functions for a step-change in temperature .	46
Table 5.7:	$Nu_x Re_x^{-\frac{1}{2}}$ for linearly stretched isothermal surface ( $\chi=1$ ) with those of Jeng et al. [21] .....	51

## **Part II**

Table 2.1:	Nozzle-dimensions .....	90
Table 3.1:	Average operating conditions during experimental runs .....	99

## LIST OF FIGURES

### **Part I**

Figure 2.1:	Coordinate system and description of physical model .....	7
Figure 4.1:	Coordinate system and physical model description .....	30

### **Part II**

Figure 2.1:	Experimental thruster and nozzle diagram .....	89
Figure 2.2:	Converging and diverging control thruster nozzle diagram .....	90
Figure 2.3:	Probe 1 with opposing static taps to measure plume flow angles	91
Figure 2.4:	Probes 2 and 3 for measuring gas impingement on a surface .....	91
Figure 2.5:	Nozzle-probe configuration .....	92
Figure 2.6:	Experimental flow system and test-cart flange .....	93
Figure 3.1:	Local flow angles for Runs 1 and 2 before correction of initial position error .....	103
Figure 3.1a:	Local flow angles for Runs 1 and 2 after correction of initial position error .....	103
Figure 3.2:	Local flow angles for Run 3 before correction of initial position error .....	104
Figure 3.2a:	Local flow angles for Run 3 after correction of initial position error .....	104
Figure 3.3:	Local flow angles for Run 4 before correction of initial position error .....	105
Figure 3.3a:	Local flow angles for Run 4 after correction of initial position error .....	105

Figure 3.4:	Impingement pressures for 10 mm and 20 mm	
	static taps for Run 5 .....	106
Figure 3.5:	Impingement pressures for 10 mm and 20 mm	
	static taps for Run 6 .....	106
Figure 3.6:	Impingement pressures for 10 mm and 20 mm	
	static taps for Run 7 .....	107
Figure 3.7:	Impingement pressures for 5 mm and 15 mm	
	static taps for Run 8 .....	107
Figure 3.8:	Impingement pressures for 5 mm and 15 mm	
	static taps for Run 9 .....	108
Figure 3.9:	Impingement pressures for 5 mm and 15 mm	
	static taps for Run 10 .....	108
Figure 3.10:	Impingement pressures for 5 mm and 15 mm	
	static taps for Run 11 .....	109
Figure 3.11:	Gas-surface interaction models .....	110
Figure 3.12:	Impingement pressure along probe surface at $Z = 50$ mm .....	111
Figure 3.13:	Impingement pressure along probe surface at $Z = 100$ mm .....	111
Figure 3.14:	Impingement pressure along probe surface at $Z = 150$ mm .....	112
Figure 3.15:	Impingement pressure along probe surface at $Z = 200$ mm .....	112
Figure 3.16:	Impingement pressure along probe surface at $Z = 250$ mm .....	113
Figure 3.17:	Impingement pressure along probe surface at $Z = 300$ mm .....	113
Figure 3.18:	Impingement pressure along probe surface at $Z = 350$ mm .....	114
Figure 3.19:	Impingement pressure along probe surface at $Z = 400$ mm .....	114

## NOMENCLATURE

### **Part I**

$a(\xi)$	universal wall velocity gradient, $f_1''(\xi, 0)$
$b(\xi)$	defined in equation (4.26 b)
$c$	constant defined in equation (4.26 a)
$c_f$	local friction coefficient defined in equation (3.25)
$\text{erfc}(x)$	complimentary error function
$f$	dimensionless stream function defined in equation (2.10)
$f_i, \theta_i$	universal functions from Merk-Chao series expansion
$h$	integration step size, $\Delta \eta$
$H(x - x_0)$	Heaviside unit operator
$k$	thermal conductivity
$K$	consistency index for non-Newtonian viscosity
$L$	reference length
$n$	power-law exponent
$Nu$	Nusselt number defined in equation (5.9)
$Nu_x$	local Nusselt number defined in equation (5.14 a)
$Pr$	generalized Prandtl number defined in equation (4.9 a)
$q_s$	surface heat flux defined in equation (5.6)
$Re$	generalized Reynolds number defined in equation (4.9 b)
$T$	temperature
$u$	velocity component in the x-direction
$U_s$	surface velocity
$v$	velocity component in the y-direction
$x$	streamwise coordinate measured along surface from slot

$x_0$	location where surface temperature step-change occurs
$y$	coordinate normal to surface

### Greek Symbols

$\alpha$	thermal diffusivity
$\delta_1$	displacement thickness defined in equation (3.27)
$\delta_2$	momentum thickness defined in equation (3.28)
$\zeta$	dimensionless variable defined in equation (4.6)
$\theta$	dimensionless temperature defined in equation (4.4)
$\xi$	dimensionless variable defined in equation (2.8)
$\eta$	dimensionless variable defined in equation (2.9)
$\Lambda$	wedge parameter defined in equation (2.13)
$\Psi$	stream function
$\rho$	density
$\tau_{yx}$	shear stress defined in equation (1.1)

### Subscripts

$s$	designates surface conditions
$\infty$	designates conditions of quiescent fluid
$i$	index variable used for Merk-Chao universal functions



## **Part II**

A	area
D	diameter
$\dot{m}$	mass flow rate
P	pressure
Q	power
R	radial distance from nozzle centerline
Re	Reynolds number
T	temperature
Z	axial distance form nozzle exit-plane

## **Greek Symbols**

$\theta$	probe rotation angle
----------	----------------------

## **Subscripts**

e	designates nozzle exit conditions
i	designates nozzle inlet conditions
o	designates stagnation conditions

An Abstract of

**ANALYSES IN THEORETICAL AND EXPERIMENTAL FLUID FLOW**

Tony G. Howell

Submitted in partial fulfillment  
of the requirements for the  
Master of Science Degree in  
Chemical Engineering

The University of Toledo

March, 1996

Two independent topics, henceforth referred to as Parts I and II, are considered in this thesis. Part I constitutes a theoretical and numerical analysis to determine the momentum and heat transfer occurring in the laminar boundary layer on a continuously moving and stretching, two-dimensional sheet in a semi-infinite, quiescent non-Newtonian power-law fluid. Part II consists of experiments completed in a simulated space thruster's low-density plume for comparison with numerical predictions.

In Part I, the Merk-Chao type of series expansion is used to generate ordinary differential equations from the partial differential momentum equation in order to obtain universal velocity functions. For the problem of combined momentum and heat transfer in the boundary layer of the moving sheet, a general power series is used to describe the fluid's velocity and temperature. Appropriate transformation variables are presented to solve the energy equation for a step-change in surface temperature. The universal functions

arising from the momentum and energy equations' solutions are numerically solved by a fourth-order Runge-Kutta technique with the Newton-Raphson subroutine controlling the iteration process. The values are compared with Jeng et al. [21] for the case of a Newtonian fluid.

Part II of this thesis experimentally investigates the local flow angles and impingement of a low-density plume using a conical probe and two  $100^\circ$  impingement cones. Both monatomic and diatomic propellants are investigated. The plume originates from a simulated space control thruster that has a 100:1 area ratio. Comparisons with direct-simulation Monte Carlo numerical predictions are also presented.

## **Part II**

### **An Experimental Analysis of Low-Density Plume Flow Angles and Impingement for Code Validation**

## **CHAPTER I**

### **Introduction**

#### **1.1 Introduction to Electrothermal Thrusters**

Satellites are most effective when orbiting at a proper orientation to the Earth; consequently, resistojets, small electrothermal propulsive devices, are frequently used to correct any deviations from proper orientation. These thrusters are in the proximity of sensitive instruments such as yaw and pitch sensors and solar arrays. Moreover, as Dettleff detailed [1], contaminants located in the plumes of these thrusters may impinge upon sensitive instruments causing malfunction or even failure. A secondary effect, unintended torques, may result from the force exerted by the gas impinging on a satellite surface.

#### **1.2 Previous Experimental and Numerical Studies**

To evaluate this problem of plume impingement, a numerical and experimental study was initiated at the NASA Lewis Research Center in Cleveland, Ohio. Using a simulated space control thruster, aspects of plume flow and background pressure effects are being investigated. To insure that the throat Reynolds number of the experimental thruster simulated actual low-thrust rockets, comparisons were made with previous investigations. Yoshida et al. [2] determined that throat Reynolds numbers of typical resistojet thrusters are around 1000. In 1991, Manzella [3] studied background pressure effects on two simulated space control thrusters. From his work, Manzella concluded that to simulate space conditions in a vacuum facility, the background pressure should be less than 0.0133 Pa. In 1993, Meissner [4] discovered that both the Reynolds number and

background pressure conditions could not be met for the experimental apparatus at NASA Lewis. Consequently, an experimental compromise was achieved. Meissner kept the throat Reynolds number at 860 and test cell pressure at 0.03 Pa, and concluded that this compromise would yield useful experimental data.

Measuring flow angles in the low-density plume of small rockets has been previously investigated by Bailey [5] and Stephenson [6]. However, the numerical modeling of the recorded data always posed difficulties. The uniqueness of the NASA Lewis effort is in the experimental/numerical design and development of the simulated resistojet where the numerical problems inherent in the previous investigators' works were minimized by the combined efforts of the experimental and numerical researchers.

Plume impingement on surfaces has been previously investigated by Legge [7] and Lengrand et al. [8]. However, Legge examined only unheated nozzle flow impinging on an inclined surface. Lengrand et al.'s investigations had throat Reynolds numbers of approximately 10000. Reynolds numbers of this magnitude are not representative of typical resistojet operation.

Part I of the experimental research began in October of 1993. While Meissner's work consisted of a diatomic propellant, nitrogen, as the exhaust plume gas, the current research of plume flow angles used a monatomic propellant, argon. Flow angles were recorded for argon at 700 K at various locations in the near-field exhaust plume.

Part II of the experimental program began in May of 1994. Pressure measurements were made along the surface of a conical impingement probe that was translated along the axis of the resistojet's exhaust plume. The measurements were made for heated and unheated flow of a diatomic propellant, nitrogen. Opposing static taps located at various distances from the conical tip were balanced to determine the static pressure readings. The preliminary results of the impingement work have already appeared in the literature [9]. However, further impingement studies have been completed since and are presented herein.

### **1.3 Contents of this Study**

The contents of this investigation describe the experimental research effort by the author at the NASA Lewis Research Center. Flow-angle data for a monatomic propellant from an electrothermal thruster and impingement data of a diatomic propellant on a conical probe will be discussed in detail. The data was taken in the nozzle exit-plane and in the near-field plume region. An analysis to approximate the experimental uncertainty for both flow-angle and impingement-pressure measurements is provided. Also, a comparison of experimental and numerical results for code validation is presented. A discussion of the experimental work along with concluding remarks and recommendations for future investigations is also given.

## **CHAPTER II**

### **Experimental Apparatus, Procedure, and Uncertainty**

#### **2.1 Experimental Apparatus**

The experimental research effort was conducted in Tank 5 at the NASA Lewis Research Center in Cleveland, Ohio. The cylindrical Tank 5 has a diameter of 4.9 meters and a length of 19 meters. Attached to the tank is one of several 0.9-meter diameter spools into which the cart with the experimental apparatus is inserted. The vacuum in the tank is maintained by twenty 0.8 meter oil-diffusion pumps and four roughing pumps. Finke et al. [10] provides a more descriptive outline of the test facility. The test-cell experimental apparatus consists of a heated thruster and nozzle, flow-angle and impingement probes, and translational tables. The flow system consists of a K-bottle, an accumulator, flow controller, and meter.

The thruster and nozzle used in the current work were designed specifically to expedite experimental and numerical comparisons and were used in Meissner's [4] study of flow angles and pitot pressures in a nitrogen exhaust plume. The thruster was fabricated at the NASA Lewis Research Center. The thruster, as shown in Figure 2.1, was mounted to a cart flange that was connected to the aforementioned spool piece. The thruster consisted of an annular flow passage radially heated by an inner heating element. The propellant flowed through this annular region where it was heated by convection and radiation. The temperatures attained by the thruster necessitated a slip support that allowed for thermal expansion during experimentation. Although the nozzle was attached to a fixed support and experienced lower temperatures, the nozzle exit plane still moved to the extent of thermal expansion over the nozzle length.



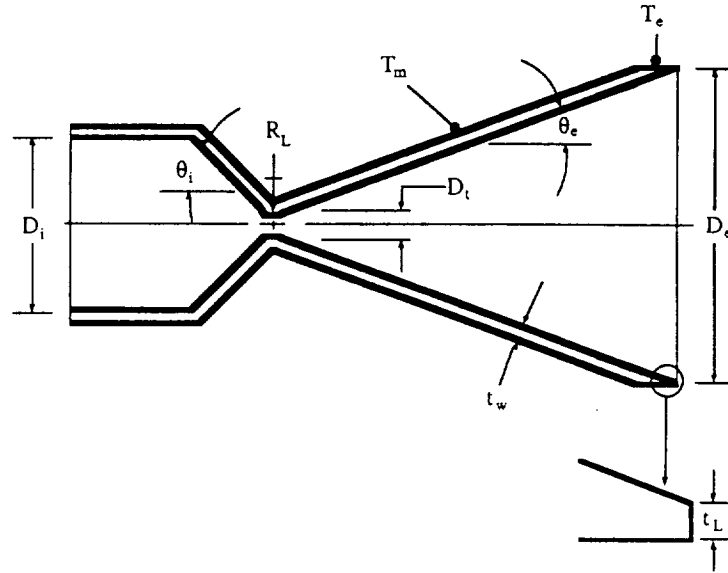


Figure 2.2: Converging and diverging control thruster nozzle diagram.

Table 2.1: Nozzle dimensions.

Exit diameter, $D_e$	31.8 mm
Inlet diameter, $D_i$	22.1 mm
Throat diameter, $D_t$	3.18 mm
Longitudinal radius, $R_L$	3.18 mm
Wall thickness, $t_w$	1.65 mm
Lip thickness, $t_L$	0.25 mm
Exit half-angle, $\theta_e$	20°
Inlet half-angle, $\theta_i$	45°
Aspect ratio	100

The conical probe used to measure flow angles was 6.35 mm in diameter with 1.0 mm diameter static pressure taps. Following the experimental procedure of Meissner [4], flow angles were determined by rotating the conical probe in the exhaust plume. Once the pressures of the opposing static taps were equal, the angle to which the probe was rotated represented the velocity flow angle at that point. Again, the size of the probe, as shown in

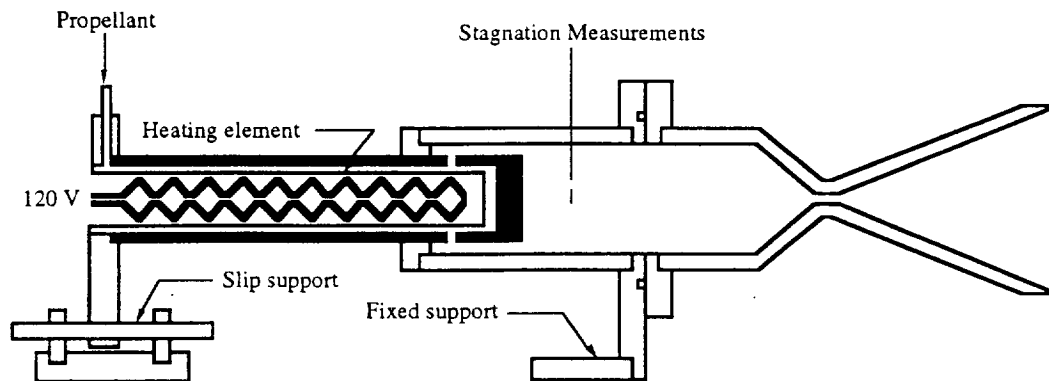


Figure 2.1: Experimental thruster and nozzle diagram.

After leaving the annular region, the propellant entered the plenum where stagnation values were recorded. The stagnation temperature was measured by a half-shielded, chromel-alumel thermocouple connected to a digital voltmeter. The stagnation pressure inside the thruster was measured by a Vacuum General capacitance manometer having a full scale of 13.3 kPa, and a listed manufacturer's accuracy of 1.0 percent of reading. From the plenum the propellant then entered the converging portion of the nozzle and exited through the divergent portion into a high-vacuum. The nozzle was designed to be large enough to minimize the probe disturbance of the plume's flow but small enough to characterize nozzles on commercial control thrusters. As shown in Figure 2.2, the nozzle had two chromel-alumel thermocouples tack-welded to the outside surface to measure mid- and exit-nozzle temperatures. The accuracy of all thermocouples was estimated to be  $\pm 2.5$  K. Important nozzle dimensions are given in Table 2.1.

Figure 2.3, was thought to be small in comparison to the nozzle exit diameter to minimize the intrusive nature of the probe.

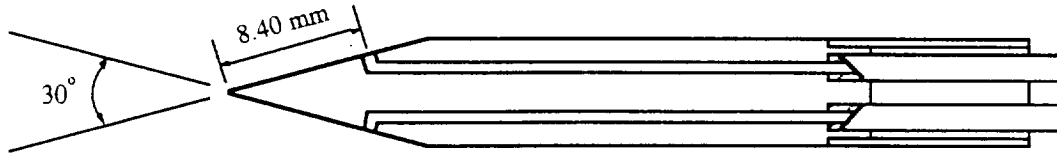


Figure 2.3: Probe 1 with opposing static taps to measure plume flow angles.

The impingement probes, as shown in Figure 2.4, were made of stainless steel and had a base diameter of 50 mm, an included angle of  $100^\circ$ , and four 1.0-mm diameter opposing static taps. The first impingement probe had static taps located 10 mm and 20 mm from the conical tip, while the second probe had the static taps located 5 mm and 15 mm along the cone's surface. Figure 2.5 illustrates the nozzle-probe configuration during experimental test runs.

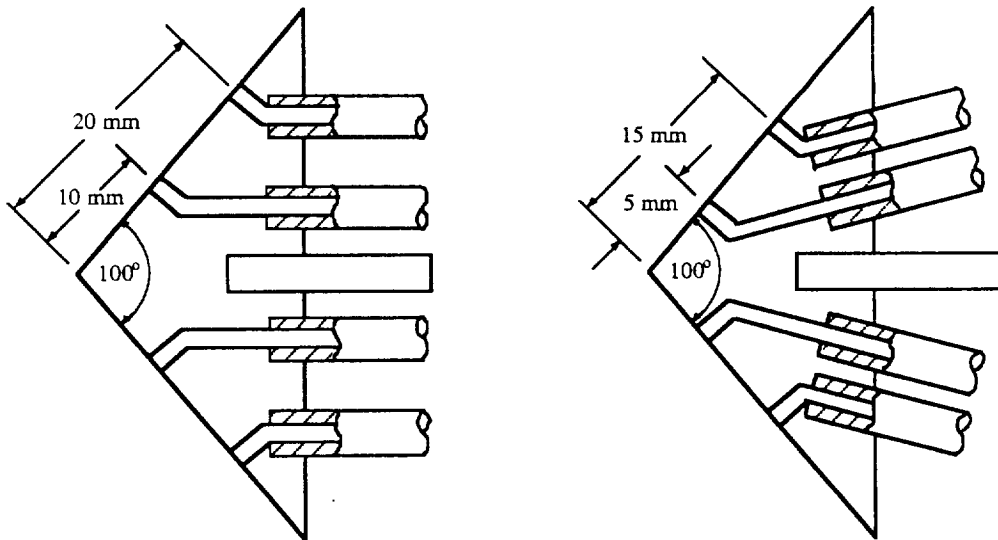


Figure 2.4: Probes 2 and 3 for measuring gas impingement on a surface.

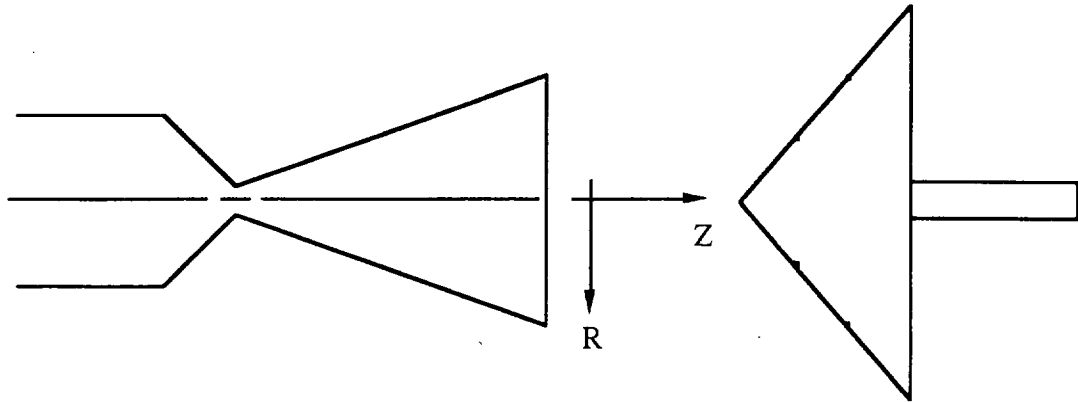


Figure 2.5: Nozzle-probe configuration.

The static taps on all the probes were connected to Vacuum General capacitance manometers having a full scale of 133 Pa, and a listed accuracy of 0.25 percent of reading. The translational tables, on which the probes were mounted, allowed for axial, radial, and rotational movement. The Compumotor 4000 step-driven tables allowed probe movement 480 mm into the plume from the nozzle exit plane and 280 mm of movement in the radial direction.

The flow system, as shown in Figure 2.6, consisted of a K-bottle, accumulator, a flow controller, and a flow meter. The K-bottle contained the propellant to be used during experimentation. A Unit Instruments flow controller with a flow meter and feedback-loop valve was used to control the flow rate. Based on calibrations performed by Meissner [4], the test flow rates were within  $\pm 3$  percent of the mass flow rate. A Teledyne-Hastings-Radist mass flow transducer that relates thermal changes to mass flow rate was used to measure propellant flow rate. The test-cell background pressure was measured by two Veeco Instruments' ionization gauges, one located inside the spool piece and the other located at the far end of Tank 5. These pressures were recorded several times throughout the experiment and a time average taken.

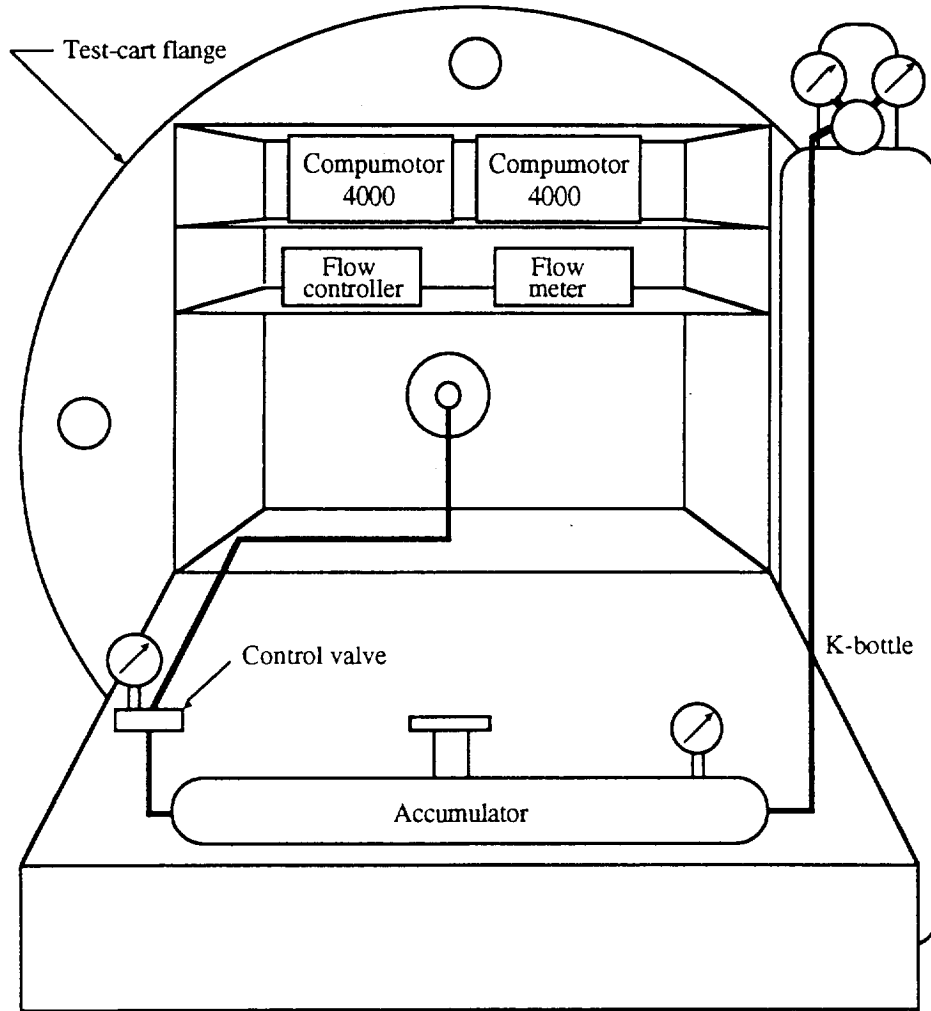


Figure 2.6: Experimental flow system and test-cart flange.

## 2.2 Experimental Procedure

The experimental procedure would begin the day before an actual test run. During the preparation day, several tasks were accomplished. First, the probe was attached to the translational tables if not already mounted. The DC power supply was turned on, and the probe centered in the nozzle exit plane by means of the translational tables, levels, and right angle square. The cart was then wheeled into the spool piece and clamped vacuum tight by compressing the o-ring on the spool flange. The spool piece was then pumped down by

the roughing pumps to a pressure close to the main tank pressure, and then the valve between the tank and spool piece was opened. The capacitance manometers were left to evacuate overnight to maintain thermal equilibrium, approximately 12-16 hours. Consequently, when the manometers were zeroed before the experimental run began the next day, the manometer readings were stable.

When unheated and heated flow studies were performed on the same day, the unheated flow case was run first. After taking initial tank pressure readings, the probe would be moved away from the nozzle prior the start of propellant flow. This was done to prevent any spiking of the sensitive capacitance manometers when the propellant flow was begun. The flow-controller valve was opened and set to the desired mass flow rate. As the static-tap pressure readings stabilized, preliminary data, such as tank pressure and flow-meter readings were recorded. The probe was moved back to the nozzle exit plane and rotated to balance opposing pressure taps. Flow symmetry checks were performed by Meissner [4] so that only a rotation was required. This rotational adjustment ensured that the probe was centered in the nozzle exit plane axially, radially, and rotationally. The translational tables' transducers were rezeroed and experimental data could then be recorded.

For the flow-angle probe, data were taken at various axial locations. At each axial location, several radial locations were investigated for flow angles. The probe was moved out into the plume and at each axial and radial location, the flow angle recorded. The flow angle was determined by balancing the opposing static taps on the probe. Assuming the finite distance between the static taps had no appreciable effect on the propellant flow or pressure readings, the opposing pressures were balanced by rotating the probe in place.

After unheated flow data were recorded, the heated flow portion of the experiment was begun. The heater was set to a voltage setting, usually 71-72 V, that allowed for steady propellant heating. Once the stagnation temperature reached 700 K, a process that took approximately 90 minutes, the heated flow data recording began. During the flow-

angle measurements, the capacitance manometers, although stable in the morning, would drift from zero. To minimize this drift, the conical probe was taken out of the near-field plume to a point behind the nozzle. The capacitance manometers were then allowed to fully evacuate. However, in the case that the manometers did not rezero, they were manually rezeroed. This rezeroing check occurred approximately every hour and could be performed during the flow-angle survey because only the flow angle was being recorded and not the absolute pressure; consequently, the rezeroing could not be done during the impingement studies.

For the impingement cones, data was taken at various locations along the plume's centerline. The impingement cones were rotated to balance opposing pressure taps at each axial location. After the daily experimentation was complete, final readings of tank and stagnation pressure and mid- and exit-nozzle temperatures were recorded. The power to the heater was then turned off, and the heating element was allowed to cool to a temperature below 400 K. The propellant flow through the thruster was maintained to expedite the cooling process, which normally took 45 minutes.

### **2.3 Uncertainty**

To provide a measure of the accuracy of the experimental results, a procedure to quantify the uncertainty is presented. Attempts were made to minimize possible errors in the experimental procedure and data recording. The following describes possible sources of errors and quantifies them to give an approximate uncertainty.

The largest source of error occurred during the preparation day when the probes were centered in the nozzle exit-plane with an index card and the eye of the author. The tip of the probe was placed on a line of the card, and the probe was translated into the nozzle exit-plane. The nozzle outline was viewed through the card, and the probe's position adjusted until the probe appeared to be centered. Thus, when the probes were moved along the plume's axis of symmetry, they actually were not exactly on the nozzle centerline. This

initial positioning error was approximated to be  $\pm 1$  mm in both the axial and radial directions.

### 2.3.1 Local Flow Angles

When the conical probe was placed on the plume centerline, the probe had to be rotated to balance the pressure readings of the opposing static taps. The largest angle of probe rotation on the axis was  $4.1^\circ$  at  $Z = 160$  mm. In the following section, graphs are presented to illustrate the local flow angle data collected. However, for each axial distance, two graphs are given. The first graph presents the actual data reading during the run, while the second graph corrects for the offset of flow angle along the axis. Finite difference schemes were used to approximate local flow angle and pressure gradients.

The uncertainty analysis was performed on two locations in the flow-angle study. The points were selected based on high and low axial and radial pressure gradients. Point A was located 36 mm from the nozzle exit-plane and 25 mm radially off the plume axis. Point B was located 120 mm from the nozzle exit-plane and 40 mm off the plume axis.

The axial and radial flow-angle gradients at point A were calculated to be  $-0.4^\circ/\text{mm}$  and  $1.2^\circ/\text{mm}$ , respectively. Multiplying these gradients by the initial positioning error of  $\pm 1$  mm, the uncertainties in axial and radial flow angle become  $\pm 0.4^\circ$  and  $\pm 1.2^\circ$ , respectively. An additional uncertainty arises from the conical probe's local flow-angle resolution. The technique of rotating the conical probe to determine the flow angle was by no means an exact procedure. Therefore, the resolution of the flow-angle probe was estimated to be  $\pm 0.5^\circ$ . Also, at point A, the conical probe had to be rotated  $0.5^\circ$  on the plume centerline which provided additional uncertainty. Summing these values, the total flow angle uncertainty at location A becomes  $0.5^\circ \pm 2.1^\circ$ .

Repeating this procedure with location B, the axial and radial flow angle gradients are  $-0.1^\circ/\text{mm}$  and  $0.4^\circ/\text{mm}$ , respectively. When multiplied by the uncertainty in the initial position, the axial and radial flow angle uncertainties become  $\pm 0.1^\circ$  and  $\pm 0.4^\circ$ . At this



location, the probe had to be rotated  $3.7^\circ$  on the plume axis. Summing these uncertainties with the conical probe's resolution of  $\pm 0.5^\circ$ , the total flow angle uncertainty at point B becomes  $3.7^\circ \pm 1.0^\circ$ .

### 2.3.2 Impingement Pressures

For the impingement study, point C was located 100 mm from the nozzle exit-plane and pressure was recorded during an unheated run at the 15 mm static tap. Point D was located 350 mm from the exit-plane and pressure was measured during a heated run at the 15 mm tap. As in the flow angle investigation, when the impingement probe was placed on the plume axis, the probe had to be rotated to balance the opposing static taps.

At location C, the axial and radial pressure gradients were evaluated to be -0.10 Pa/mm and -0.40 Pa/mm, respectively. When multiplied by the initial position uncertainty of  $\pm 1$  mm, the axial and radial static pressure uncertainties become  $\pm 0.10$  Pa and  $\pm 0.40$  Pa, respectively. Moreover, at location C, the probe had to be rotated approximately  $4.0^\circ$ . This added another  $\pm 1$  mm uncertainty in both the axial and radial directions. Consequently, the uncertainty in the static pressure measurement at location C is  $\pm 1.0$  Pa. This constitutes an error of approximately 12%. Moreover, the listed accuracy of the capacitance manometer was 0.25% of the pressure reading. Therefore, the total uncertainty at location C is  $\pm 1.02$  Pa or 12.3%. The static pressure measurement at location C is between 6.74 Pa and 8.78 Pa ( $7.76 \pm 1.02$  Pa).

The uncertainty at location D was less than location C due to the lower pressure gradients in the plume. The axial and radial pressure gradients at location D were determined to be -0.004 Pa/mm and 0.003 Pa/mm, respectively. Using the position uncertainty of  $\pm 1$  mm, the axial and radial static pressure uncertainties become  $\pm 0.004$  Pa and  $\pm 0.003$  Pa, respectively. At this location, the impingement probe had to be rotated  $10^\circ$ , which added  $\pm 2$  mm in axial and radial impingement pressure uncertainty. Thus, the static pressure uncertainty at location D is  $\pm 0.021$  Pa or 2.2%. Adding the capacitance

manometer listed accuracy of 0.25%, the total static pressure uncertainty at location D is  $\pm 0.023$  Pa or 2.5%. Therefore, the static pressure at location D is in the range 0.94 Pa to 0.98 Pa ( $0.96 \pm 0.023$  Pa).

The 15-mm tap was chosen for the uncertainty analysis because of ease in evaluating axial and radial pressure gradients. Readings involving the static pressure tap 10 mm from the tip were believed to include additional uncertainty. When these runs were performed, only three capacitance manometers were functioning. Two of the capacitance manometers were connected to the static taps located 20 mm from the probe tip while the other manometer was connected to one of the 10 mm taps. Although static pressure measurements were recorded for the 10 mm tap, there was no opposing static tap to balance to ensure accurate data. Therefore, this uncertainty can only be approximated to be  $\pm 40\%$ .

## CHAPTER III

### Experimental Results and Discussion

#### 3.1 Run Definitions

Although only eleven runs will be described in this chapter, a total of thirteen experimental runs were performed at NASA Lewis. As detailed later, the last two runs in Tank 5 proved to have more experimental error than what could be explained. Table 3.1 lists the average operating temperature and pressure conditions and mass flow rate of the gas for each run.

Run	$\dot{Q}$ (W)	$\dot{m}$ (g/s)	$P_b$ (Pa)	$P_o$ (Pa)	$T_o$ (K)	$T_m$ (K)	$T_e$ (K)
1	65.4	0.0033	0.021	5280	700	495	487
2	64.0	0.0033	0.021	5180	700	493	487
3	64.1	0.0033	0.021	5200	700	493	486
4	64.1	0.0033	0.025	5230	700	494	486
5	66.9	0.0068	0.033	6330	700	507	499
6	0.0	0.0068	0.027	4180	300	296	295
7	66.9	0.0068	0.033	6330	700	507	499
8	0.0	0.0068	0.027	4200	305	297	297
9	67.3	0.0068	0.027	6350	700	507	499
10	0.0	0.0068	0.027	4220	308	301	301
11	67.3	0.0068	0.027	6320	700	504	496

Table 3.1: Average operating conditions during experimental runs.

The column headings in Table 3.1 are as follows:

$\dot{Q}$  - Power supplied to the cartridge heater.

$\dot{m}$  - Propellant mass flow rate.

$P_b$  - Tank pressure.

$P_o$  - Propellant stagnation pressure.

$T_o$  - Propellant stagnation temperature.

$T_m$  - Nozzle wall temperature half/way between the throat and the exit-plane.

$T_e$  - Nozzle wall temperature near the exit-plane.

Details of each experimental run are given in the following pages.

Runs 1 & 2: Flow angles in a heated argon exhaust plume were recorded with the conical probe for axial distances of 160 and 120 mm and radial distances up to 50 mm. Run 2 repeated Run 1 and the average plume flow angles from both runs are given in Figure 3.1. Figure 3.1a corrects for initial positioning error.

Run 3: Flow angles in a heated argon exhaust plume were recorded with the conical probe for axial distances of 80 and 60 mm and radial distances up to 45 mm and are given in Figure 3.2. Figure 3.2a corrects for initial positioning error.

Run 4: Flow angles in a heated argon exhaust plume were recorded with the conical probe for an axial distance of 36 mm and radial distances up to 45 mm and are given in Figure 3.3. Figure 3.3a corrects for initial positioning error.

- Run 5: Impingement pressure measurements in a heated nitrogen plume were recorded with impingement probe 1 for axial distances ranging from 50 mm to 400 mm. Two capacitance manometers were used, one on the 10 mm tap and the other on the 20 mm tap. Since these manometers were on the same side of the impingement probe, the probe could not be rotated to balance opposing static taps. The results are given in Figure 3.4.
- Run 6: Impingement pressure measurements in an unheated nitrogen plume were recorded with impingement probe 1 for axial distances ranging from 50 mm to 400 mm. Three capacitance manometers were used, one on the 10 mm tap and the other two on the 20 mm taps. The probe was rotated to balance the pressure of the opposing 20 mm taps. Results are given in Figure 3.5.
- Run 7: Impingement pressure measurements in a heated nitrogen plume were recorded with impingement probe 1 for axial distances ranging from 50 mm to 400 mm. Three capacitance manometers were used, one on the 10 mm tap and the other two on the 20 mm taps. The probe was rotated to balance the pressure of the opposing 20 mm taps. Results are given in Figure 3.6.
- Run 8: Impingement pressure measurements in an unheated nitrogen plume were recorded with impingement probe 2 for axial distances ranging from 50 mm to 400 mm. Four capacitance manometers were used, two on the 5 mm taps and the other two on the 15 mm taps. The probe was first rotated to balance the pressure of the opposing 5 mm taps and then the 15 mm taps. Results are given in Figure 3.7.

- Run 9: Run 8 was repeated with a heated nitrogen plume. Results are given in Figure 3.8.
- Run 10: Run 8 was repeated. Results are given in Figure 3.9.
- Run 11: Run 9 was repeated. Results are given in Figure 3.10.
- Run 12: The impingement study was expanded by investigating unheated nitrogen plume impingement on a flat circular disk with static pressure taps located approximately 8 mm and 20 mm from the center of the disk. Four capacitance manometers were used, two on the 8 mm taps and the other two on the 20 mm taps. To balance the pressures of the opposing static taps during the experiment, the probe had to rotated in excess of 30 degrees. This probe rotation was not within experimental uncertainty; consequently, the data is not presented in this work.
- Run 13: Run 12 was repeated for heated nitrogen flow, with similar results.

### 3.2 Experimental Results

The following figures present the experimental data recorded at the NASA Lewis Research Center.

#### 3.2.1 Argon Local Flow Angles

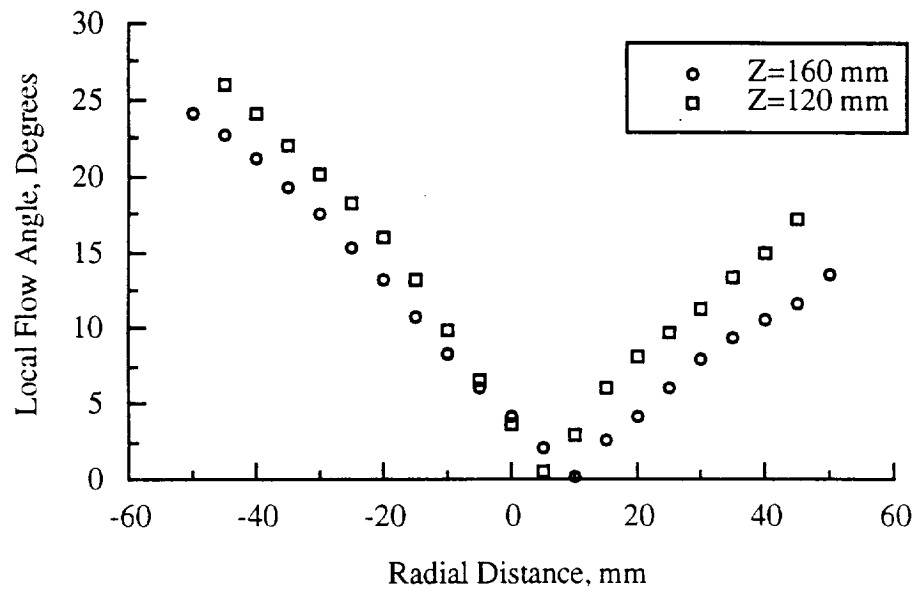


Figure 3.1: Local flow angles for Runs 1 and 2 before correction of initial position error.

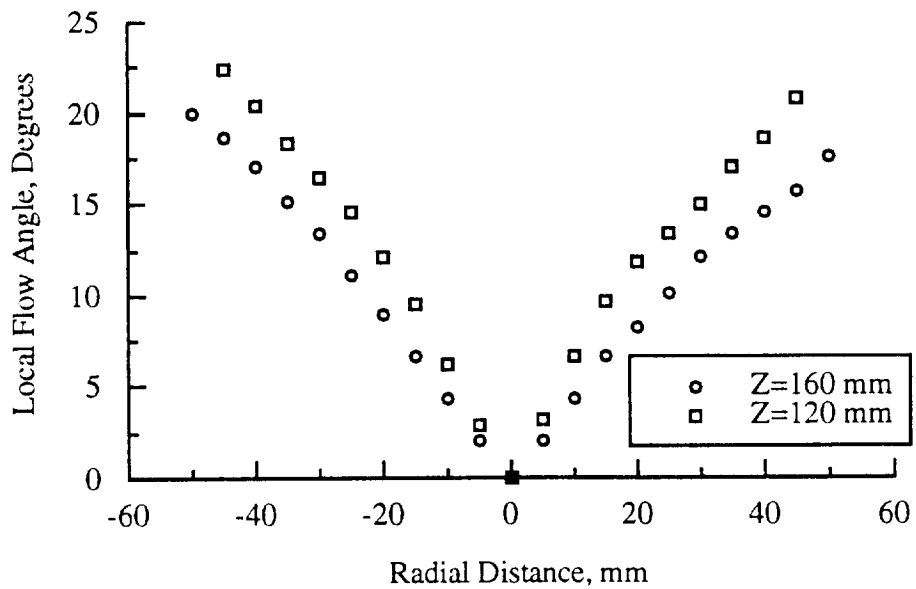


Figure 3.1a: Local flow angles for Runs 1 and 2 after correction of initial position error.

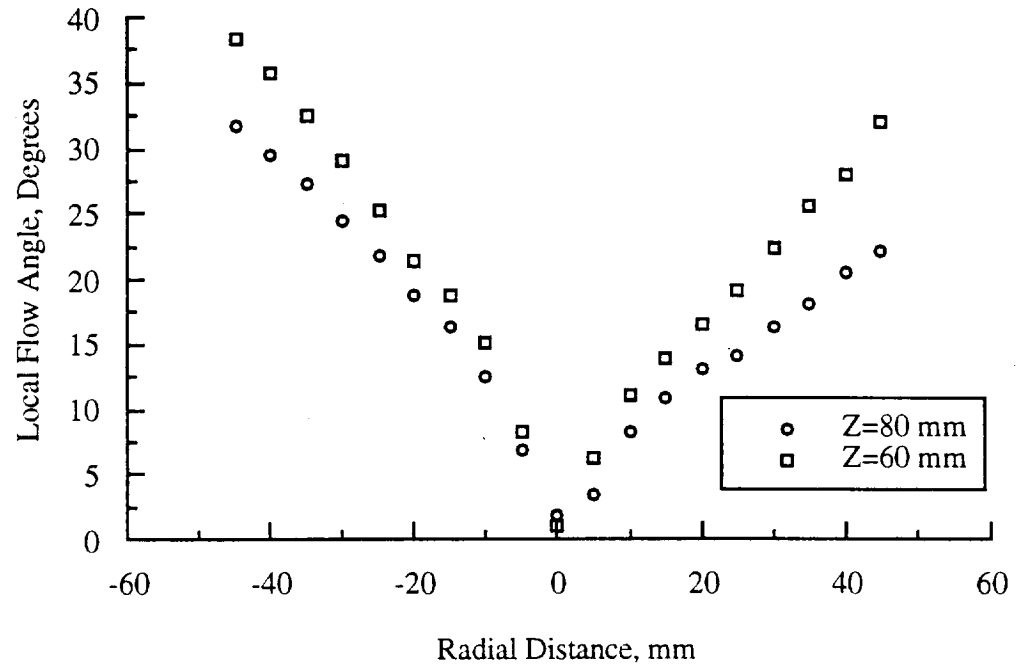


Figure 3.2: Local flow angles for Run 3 before correction of initial position error.

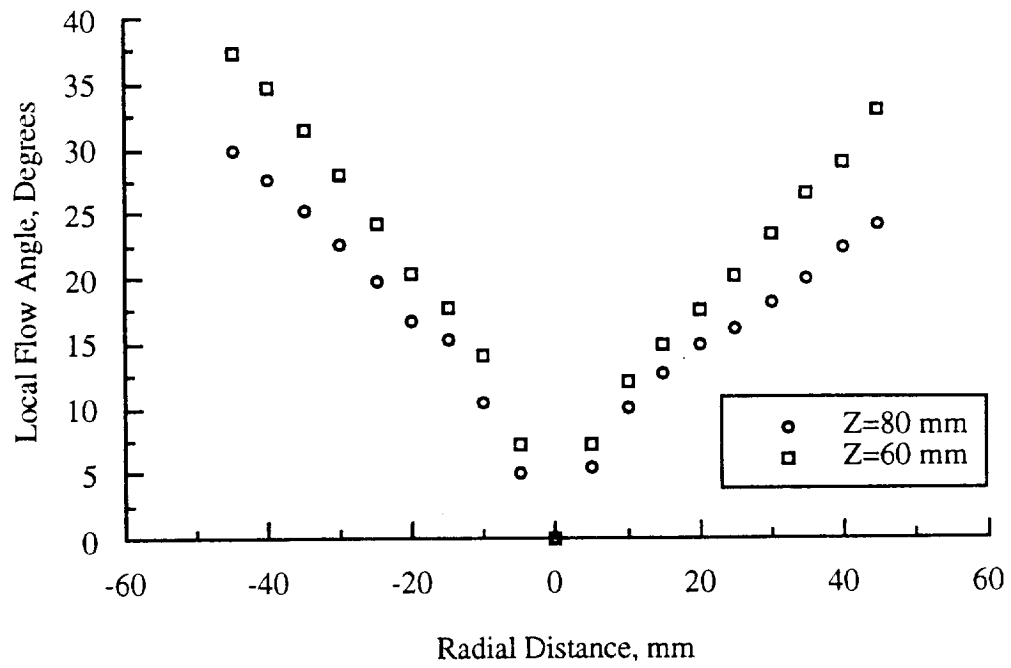


Figure 3.2a: Local flow angles for Run 3 after correction of initial position error.



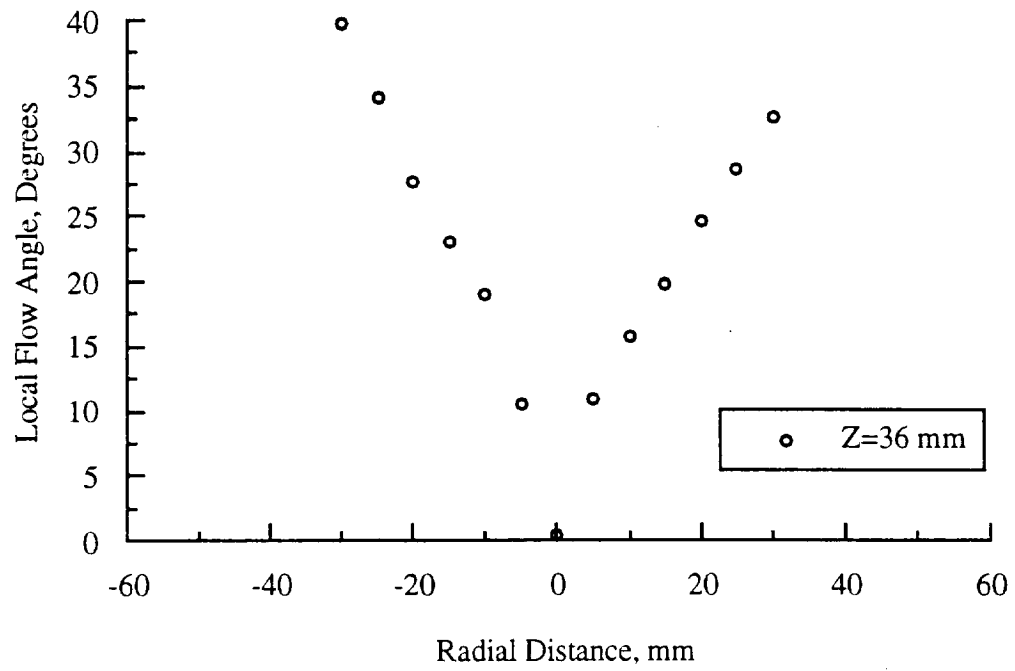


Figure 3.3: Local flow angles for Run 4 before correction of initial position error.

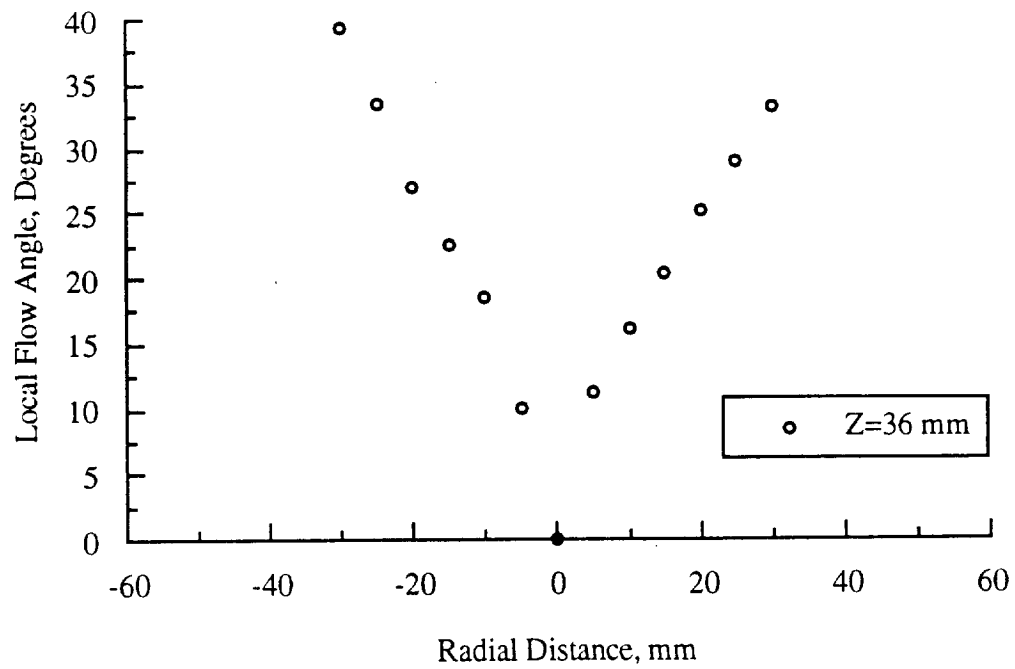


Figure 3.3a: Local flow angles for Run 4 after correction of initial position error.

## 3.2.2 Nitrogen Plume Impingement Pressures

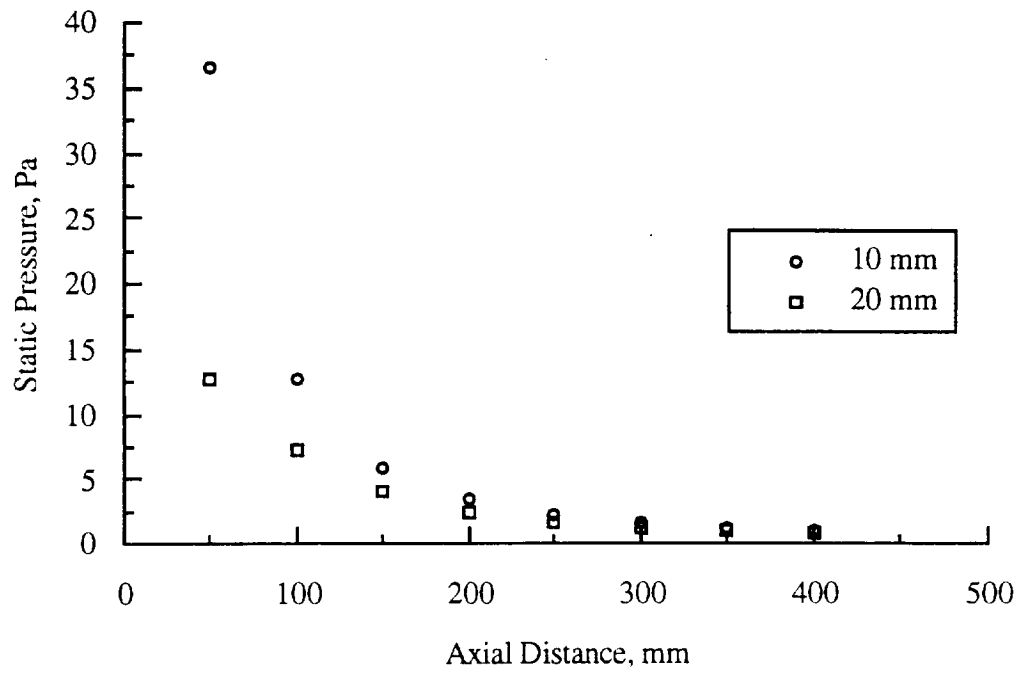


Figure 3.4: Impingement pressures for 10 mm and 20 mm static taps for Run 5.

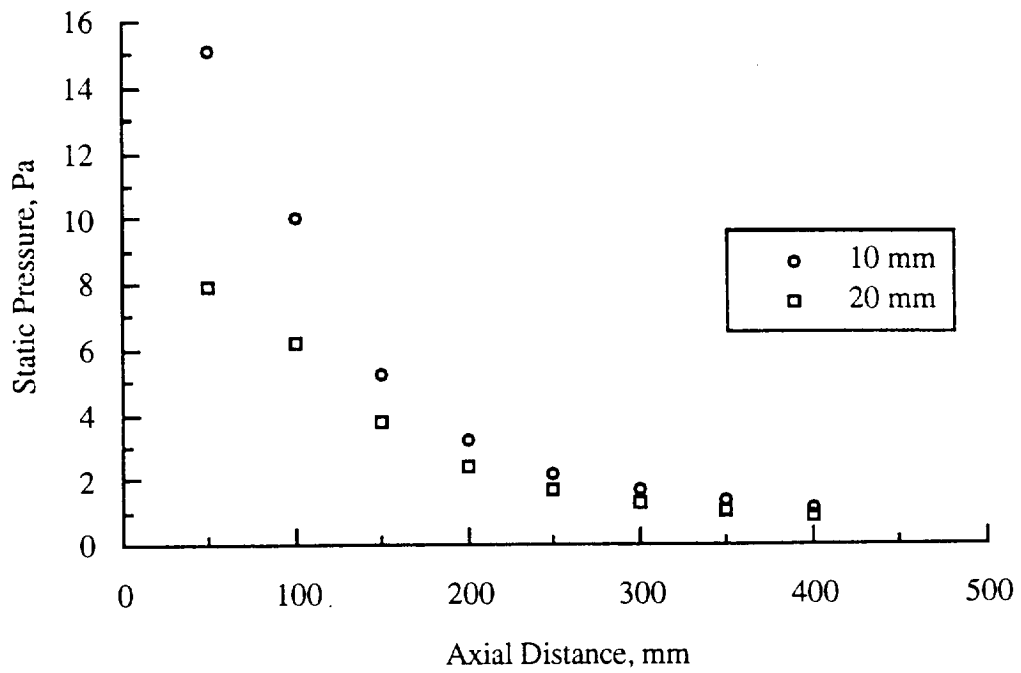


Figure 3.5: Impingement pressures for 10 mm and 20 mm static taps for Run 6.

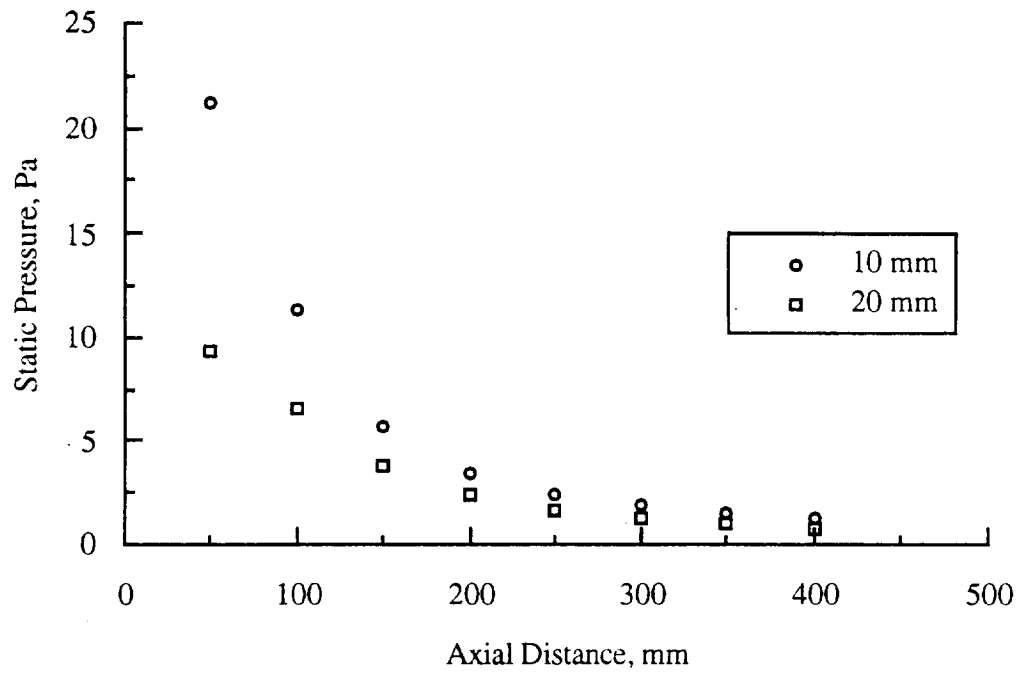


Figure 3.6: Impingement pressures for 10 mm and 20 mm static taps for Run 7.

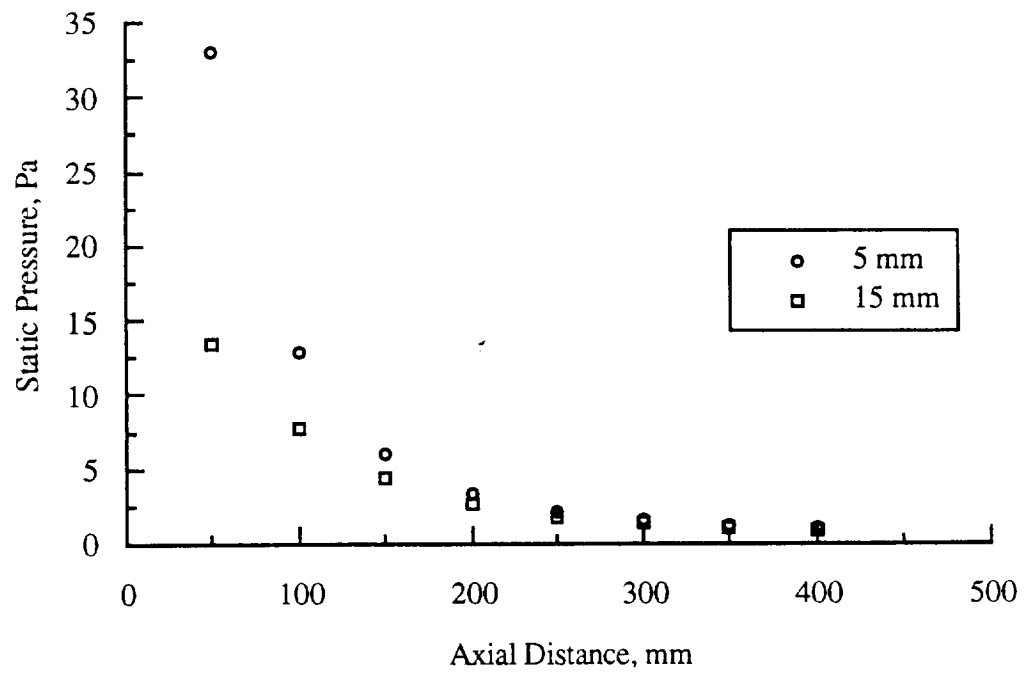


Figure 3.7: Impingement pressures for 5 mm and 15 mm static taps for Run 8.

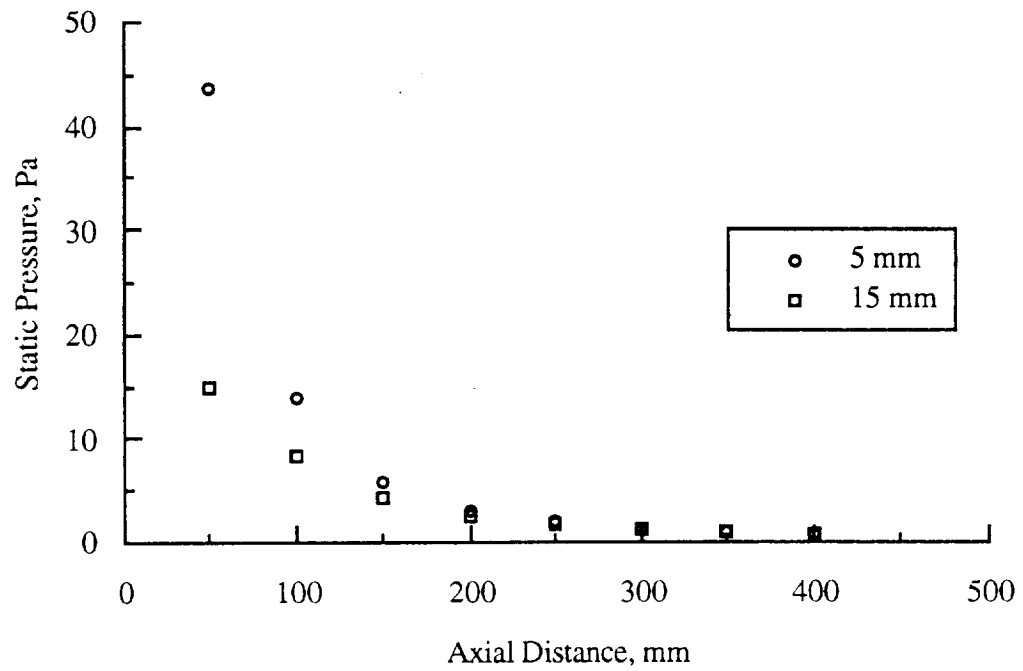


Figure 3.8: Impingement pressures for 5 mm and 15 mm static taps for Run 9.

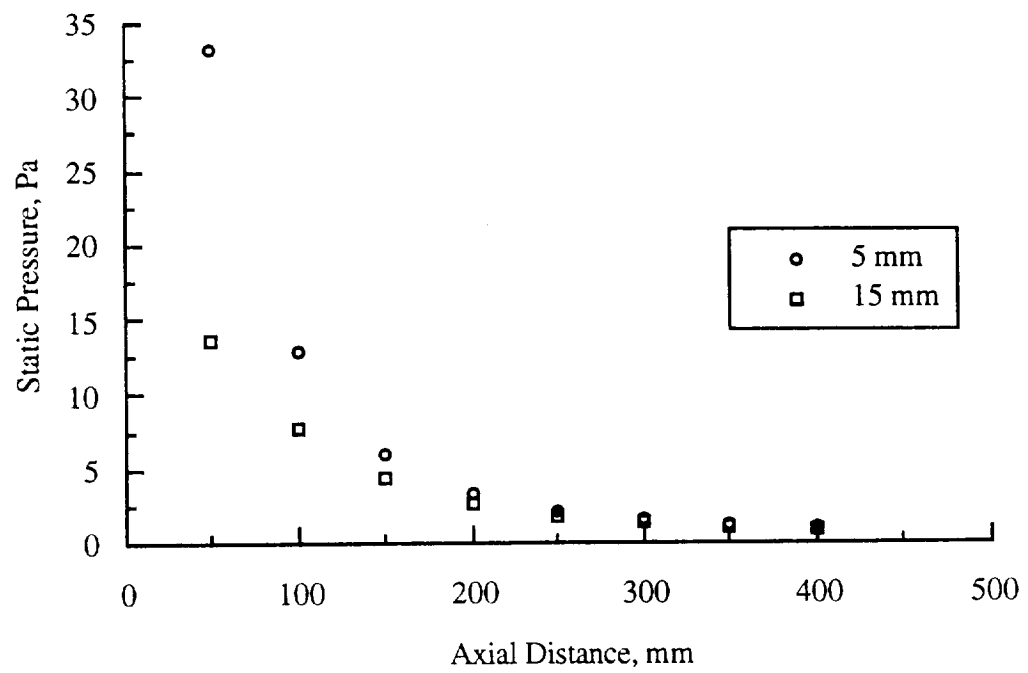


Figure 3.9: Impingement pressures for 5 mm and 15 mm static taps for Run 10.

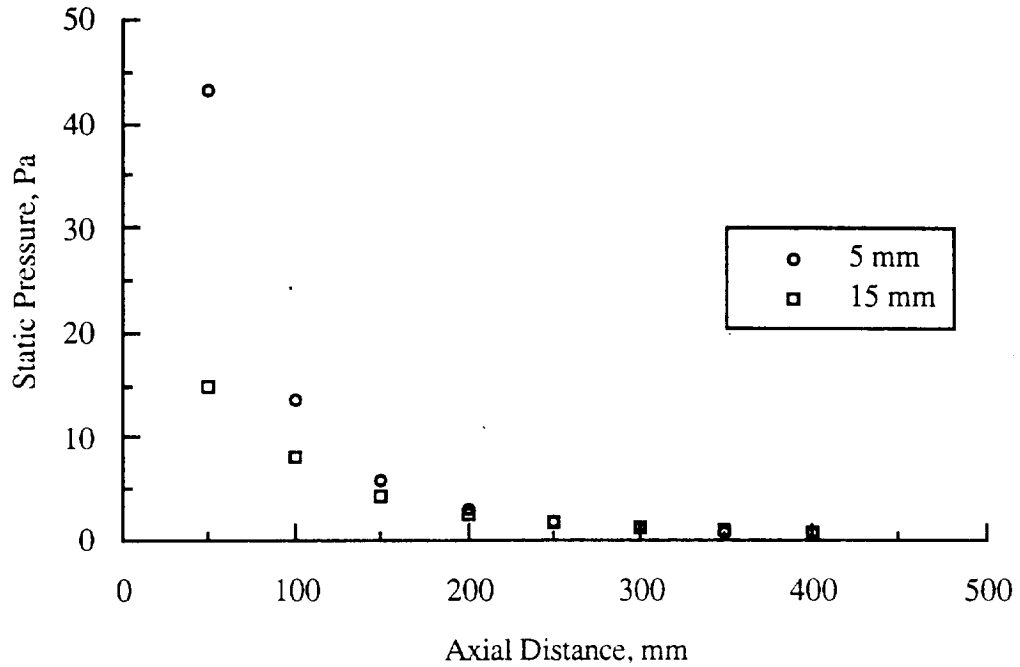


Figure 3.10: Impingement pressures for 5 mm and 15 mm static taps for Run 11.

### 3.3 Direct-Simulation Monte Carlo Results

The experimental results have already been compared to numerical predictions in the literature [9]. However, more impingement studies have been completed since that publication and are presented in this section. The numerical code uses the direct-simulation Monte Carlo (DSMC) method, developed by Bird [11], to simulate real gas flow.

The numerical code, based in kinetic theory, employs DSMC to directly calculate low-density gas flows at the molecular level. The calculations begin at the nozzle exit-plane where the gas is assumed to expand into a perfect vacuum. The nozzle exit conditions for the current study were taken from a previous study [14] which have been verified through direct comparisons with experimental data [14]. The gas flow on the centerline of the exit-plane has a Mach number of approximately 5. Consequently, at the point where the gas impinges upon the conical surface, the flow is hypersonic. The evaluation of gas impingement is not straightforward but can be aided by using simplified models.

The two models, as shown in Figure 3.11, represent the theoretical limits of gas-surface interaction. The first model, diffuse reflection, assumes full energy accommodation to the conical surface temperature which for this case is 300 K. Considering the hypersonic flow at the point of impingement, it seems unlikely that all the molecular energy will be accommodated. The second model, specular reflection, simply reverses the sign of the normal velocity component of the impinging gas.

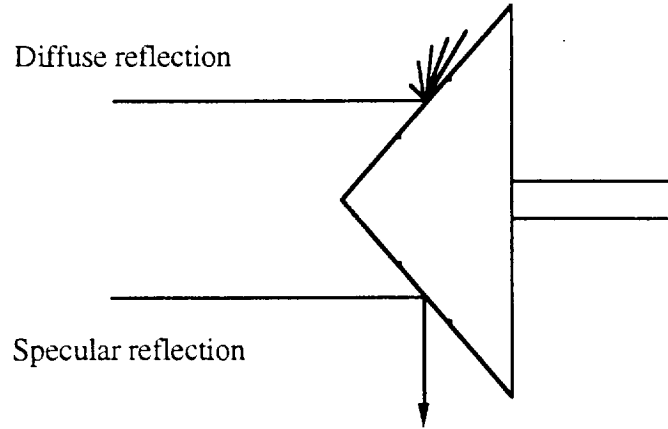


Figure 3.11: Gas-surface interaction models.

At the time of publication of the preliminary results [9], only the 10 and 20 mm pressure static tap data for heated nitrogen flow had been recorded. Impingement pressure data from the 5 and 15 mm static taps have since been recorded. These data are inserted into the graphs that appeared in the previous publication [9] and are presented here. The impingement pressure on the conical surface is calculated by the DSMC method for axial distances of  $Z = 50, 100, 200, 300,$  and  $400$  mm and is shown in Figures 3.12, 3.13, 3.15, 3.17 and 3.19, respectively. In these figures, the surface pressure obtained with the specular reflection model is lower than that calculated by the diffuse reflection model. This phenomena occurs because the specular model reflects gas particles far from the probe surface while the diffuse model produces a thin boundary layer of cool particles near the surface. Figures 3.14, 3.16, and 3.18 show only the experimental results at  $Z = 150, 250$  and  $350$  mm distances, respectively.

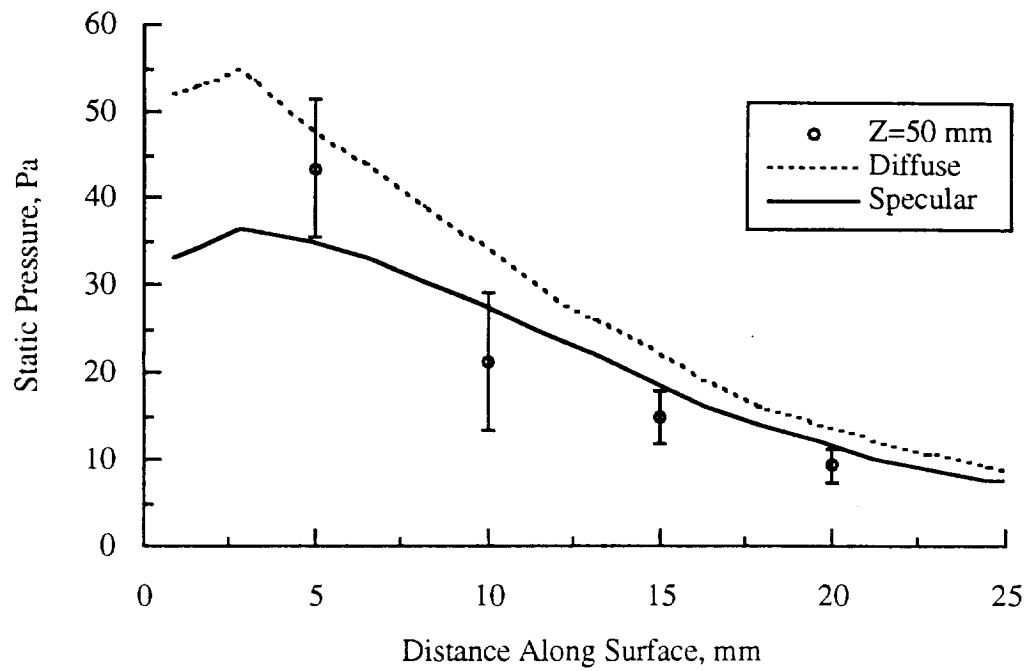


Figure 3.12: Impingement pressure along probe surface at  $Z = 50$  mm.

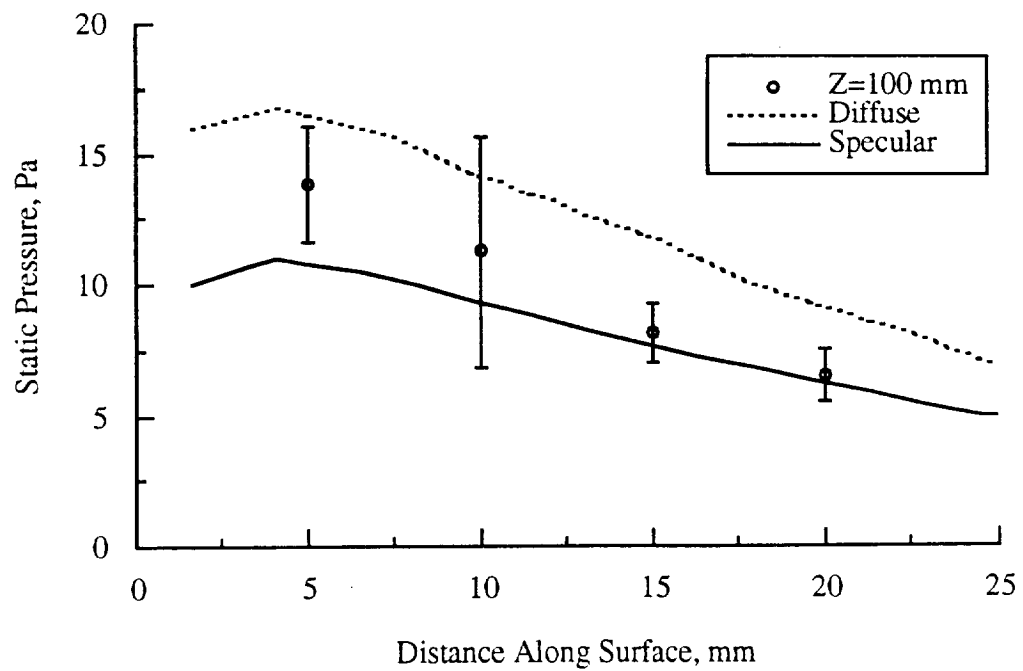


Figure 3.13: Impingement pressure along probe surface at  $Z = 100$  mm.

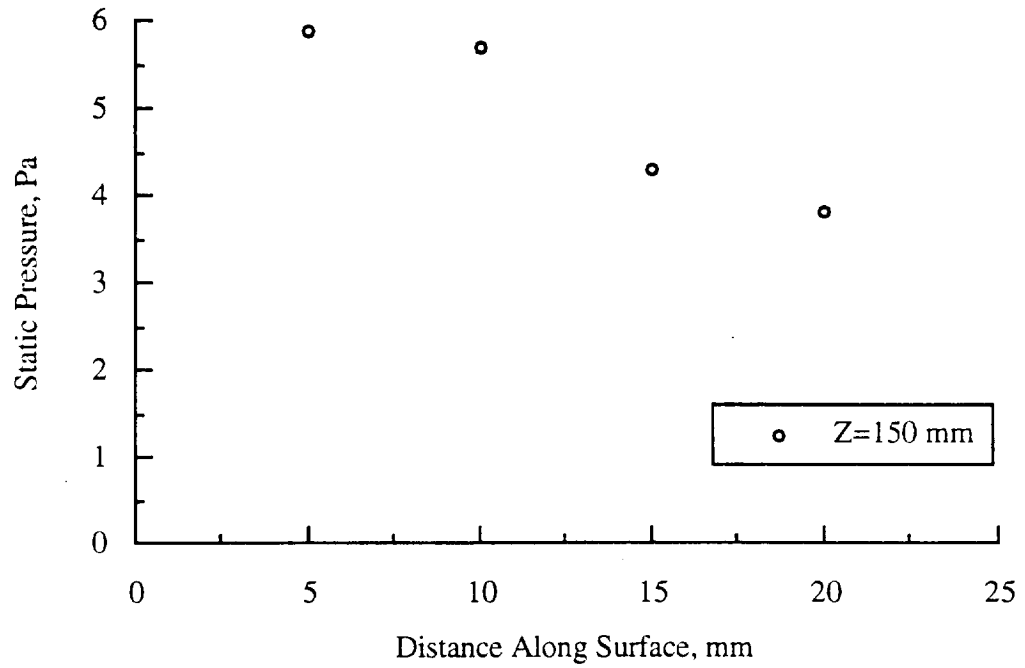


Figure 3.14: Impingement pressure along probe surface at  $Z = 150$  mm.

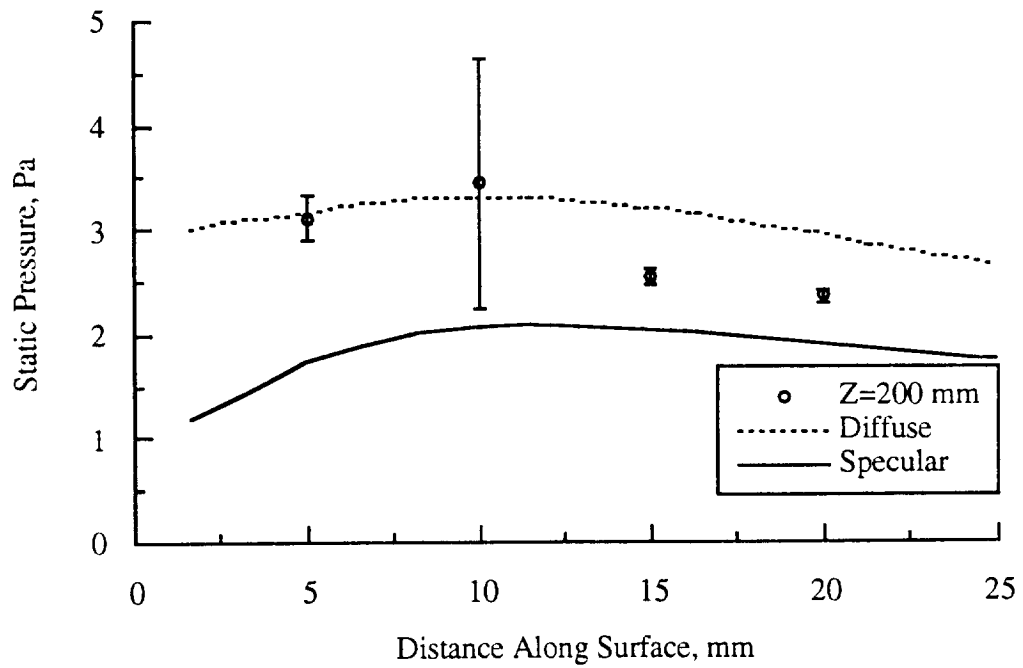


Figure 3.15: Impingement pressure along probe surface at  $Z = 200$  mm.



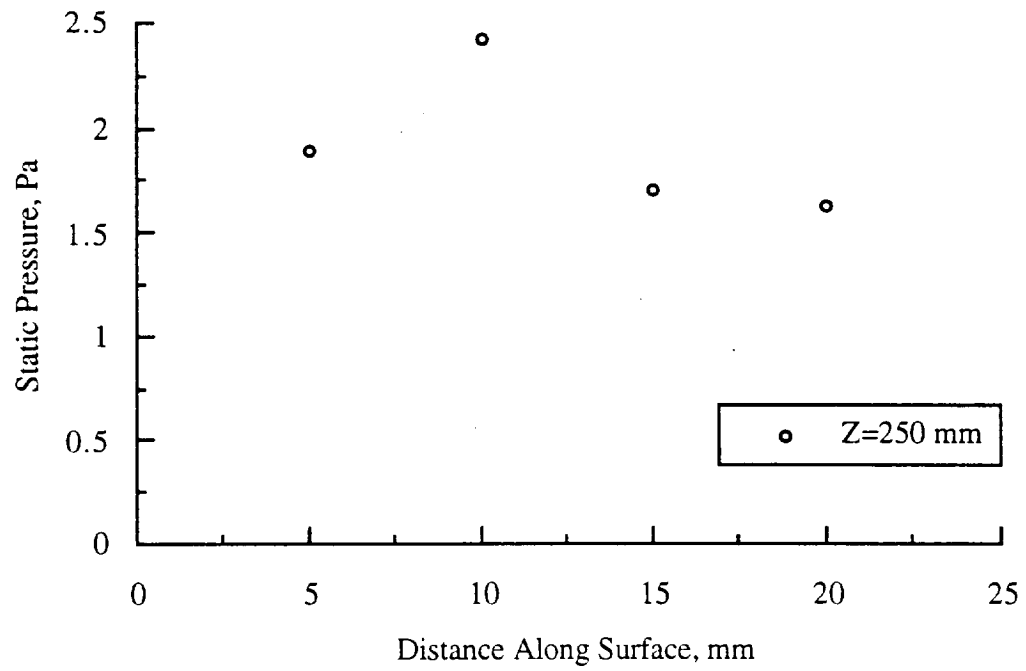


Figure 3.16: Impingement pressure along probe surface at  $Z = 250$  mm.

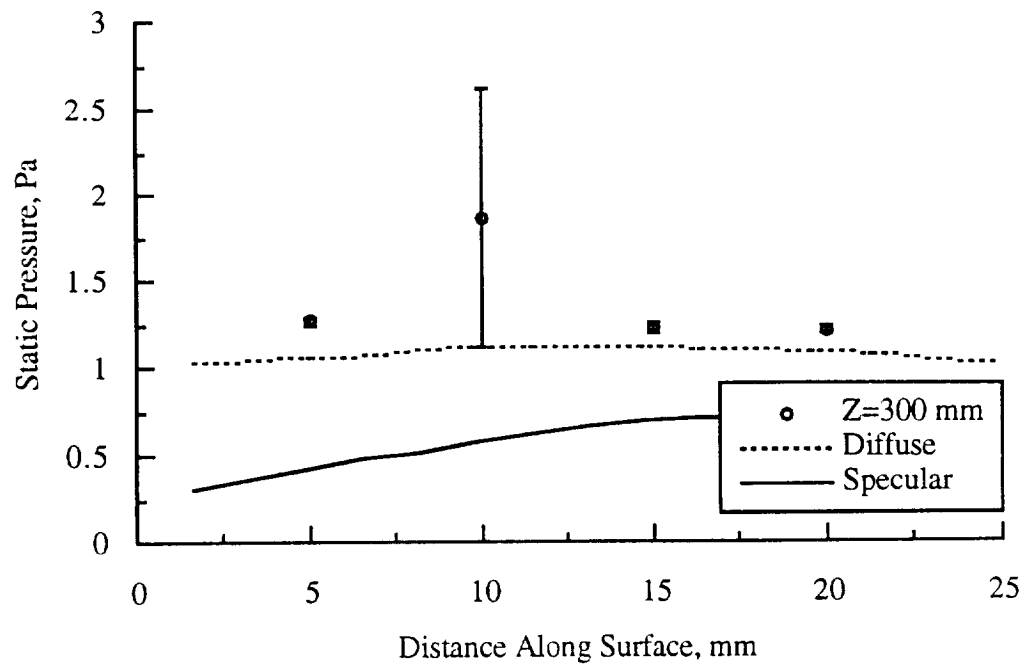


Figure 3.17: Impingement pressure along probe surface at  $Z = 300$  mm.

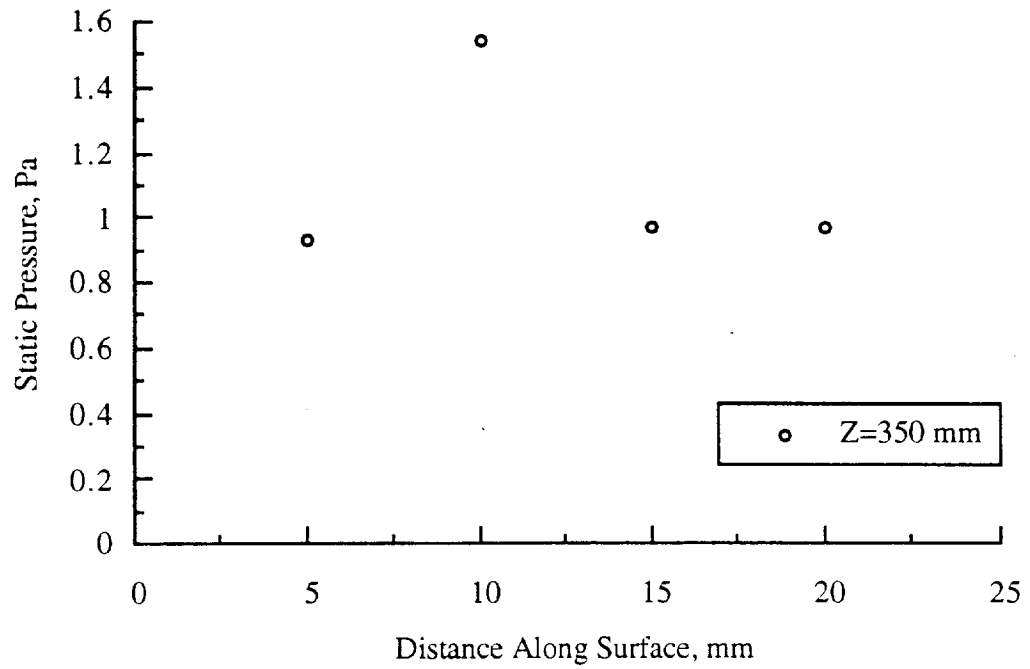


Figure 3.18: Impingement pressure along probe surface at  $Z = 350$  mm.

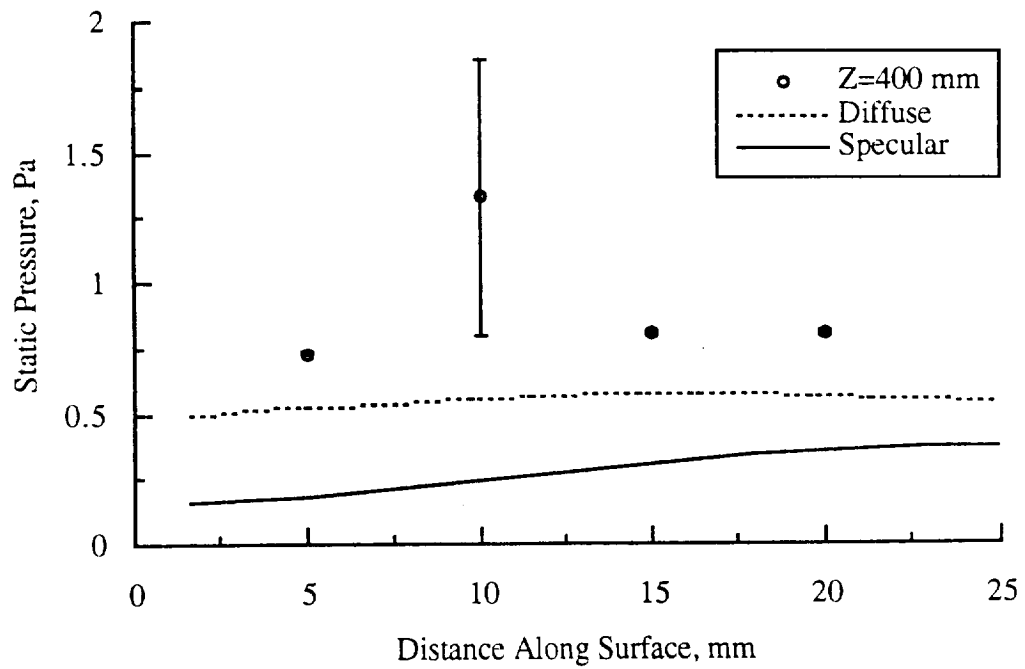


Figure 3.19: Impingement pressure along probe surface at  $Z = 400$  mm.

### 3.4 Discussion

Although Figures 3.1 and 3.1a show averages of runs 1 and 2, the local flow angles of an argon plume recorded during both runs were within the experimental uncertainty. The unsymmetrical flow angles shown in Figure 3.1 are from the initial positioning uncertainty during preparation. In Figure 3.1, the plume axis appears to be 10 mm to the right at  $Z = 160$  mm. This does not mean that the initial center positioning in the nozzle exit-plane was off by 10 mm. Most likely, the error was on the order of  $\pm 1$  mm, and as the distance between the conical probe and nozzle exit-plane increased, so did the magnitude of this uncertainty.

Runs 3 and 4 were not repeated, so a comparison with similar runs is not possible. However, all figures, 3.2, 3.2a, 3.3, and 3.3a, show good symmetry because the conical probe was rotated less than  $2^\circ$  at  $Z = 80, 60$ , and  $36$  mm. Even though centerline flow angle corrections were made to better illustrate the local flow angles in the argon plume at all axial locations, the plume appears to be slightly unsymmetrical. At all axial locations, the local flow angles on the left side of the plume were greater than those on the right. Again, this can be attributed to experimental error, a slight machining error in nozzle fabrication, and possible misalignment of the thruster.

In run 5, the probe, propellant, and scope of the experiment were changed. The purpose of the impingement study was to investigate nitrogen plume impingement on a cone. As shown in Figure 3.4, the impingement pressure decreases as the distance between the probe and the nozzle exit-plane increases. Also, the 10-mm static tap experienced higher pressures than the 20-mm static tap at all axial locations. Even though the 10-mm static tap had a larger uncertainty, it can not be seen from run 5. It is worth noting that only two capacitance manometers were available for run 5. One manometer was connected to the 10-mm tap and the other to the 20-mm tap; consequently, the opposing static taps could not be balanced to ensure alignment of the probe.

In run 6, three capacitance manometers, two connected to the 20-mm taps and one connected to the 10-mm tap, were used to measure impingement pressures in an unheated nitrogen plume. The impingement pressures were less than those found in run 5 even though the mass flow rate of the two runs was the same. Figure 3.5 shows the difference in the impingement pressure that can be attributed to the heat added in run 5. The energy added to the propellant in the thruster increases its impingement pressure on the cone.

Run 7 repeated run 5. A comparison of the impingement pressures in Figures 3.4 and 3.6 recorded during runs 5 and 7 at both 10- and 20-mm taps show a decrease when the probe was rotated to balance the 20-mm taps. From this comparison, one can conclude that during run 5 the side of the probe that the manometers were connected was angled toward the nozzle; thus, higher pressures were recorded during run 7.

Run 8, illustrated in Figure 3.7, used four capacitance manometers and the second impingement cone that had static pressure taps located 5- and 15-mm from the tip. At each axial location, the probe was rotated to balance the pressure readings of the 5-mm tap and then the 15-mm tap. Normally, the angle at which the probe was rotated to balance the 5-mm tap was not equal to the rotation angle for the 15-mm tap.

Run 9 used the second impingement probe to record static pressures in a heated nitrogen plume. As seen in Figure 3.8, the impingement pressures were higher for the heated flow than for the unheated flow. Again, the difference stems from the fact that the gas has more energy due to its higher temperatures.

Run 10 repeated run 8 and, as seen in a comparison of Figures 3.7 and 3.9, the impingement pressures from both runs were within experimental uncertainty at all axial distances. Run 11, Figure 3.10, repeated run 9, and again all data recorded were within approximated uncertainty.

Figures 3.12 through 3.19 take the recorded data and present the overall trends in a different manner. The impingement pressure along the surface of the probe, i.e., at the 5-, 10-, 15-, and 20-mm taps, are shown along with the DSMC results. Aside from the 5-mm

static tap, the experimental impingement pressure in Figure 3.12 is less than both numerical model predictions. In Figures 3.13 and 3.15, the experimental pressure lies between the numerical models. However, in Figures 3.17 and 3.19, at axial distances of 300 and 400 mm, the experimental impingement pressure is higher than model predictions. In Figure 3.12, at a distance of  $Z = 50$  mm, the impingement pressure decreases as the distance from the conical tip increases. This trend can also be seen to a lesser degree in Figures 3.13 to 3.16 when excluding the 10-mm data point. In Figures 3.17 and 3.18, the impingement pressure remains almost constant along the conical surface except for the 10-mm tap. Again, it is worth noting that the pressure readings of the 10-mm tap have a larger experimental uncertainty than other static tap readings. Figure 3.19 shows that the impingement pressure actually increases as the distance from the conical tip increases.

Preliminary experimental and numerical results have already appeared in the literature [9] and appear again in this work; however, a more robust and efficient numerical code, MONACO, has been recently developed by Kannenberg et al. [12]. This code parallelizes the computational load of the direct simulation Monte Carlo method and, thus, improves the efficiency. Also, any geometrical configuration can be handled by the software due to a flexible computational grid scheme. Although efficiency and flexibility were markedly improved, the small difference in the numerical predictions between the previous paper [9] and the more recent paper [12] did not merit another in depth comparison here.

## **CHAPTER VI**

### **Conclusions and Recommendations**

This study was part of a larger experimental/numerical investigation undertaken at the NASA Lewis Research Center on plume interaction with sensitive instruments on satellites. Local flow angles and impingement pressures were measured in argon and nitrogen low-density plumes originating from a resistojet in high vacuum. The data were taken during eleven runs in the near-field plume of the thruster and compared with DSMC predictions where possible.

The argon flow angle study used a conical probe with opposing static taps to measure the local flow angle. By rotating the probe at various axial and radial locations and balancing the pressure readings of the opposing taps, the flow angle was found. The nitrogen impingement study used two impingement cones, one with static taps located 10 and 20 mm from the conical tip and the other with taps 5 and 15 mm from the tip, to investigate plume impingement along the centerline.

An approach to approximate the experimental uncertainty was presented along with sample calculations. The uncertainties in the flow angle were found to vary between  $0.5^{\circ} \pm 2.1^{\circ}$  at a point close to the exit-plane and  $3.7^{\circ} \pm 1.0^{\circ}$  at a position further into the plume. The impingement uncertainties ranged from  $\pm 12.3\%$  of the recorded value in the near-field plume to  $\pm 2.5\%$  in the far-field plume.

It is recommended that in the future, certain aspects of this intensive experimental/numerical investigation be improved to minimize experimental uncertainty and to ensure accurate data collection. The largest source of error, the initial centering of the probe in the nozzle exit-plane, could be reduced or even eliminated if a mechanical device

or laser alignment technique was used for this critical positioning. Also, the intrusive nature of the probe could be eliminated if a laser technique, such as electron beam fluorescence developed by Rothe [13], was implemented as the major tool for data collection.

## REFERENCES

- [1] Dettleff, G., "Plume Flow and Plume Impingement in Space Technology," *Progress in Aerospace Sciences*, Vol. 28, pp. 1-71, 1991.
- [2] Yoshida, R. Y., Halbach, C. R. and Hill, S. C., "Life Test Summary and High Vacuum Tests of 10mlb Resistojets," *Journal of Spacecraft and Rockets*, Vol. 8, pp. 414-416, April 1971.
- [3] Manzella, D. H., "An Experimental Investigation of the Effect of Cell Pressure on the Performance of Resistojets," M.S. Thesis, University of Toledo, Toledo, Ohio, 1988.
- [4] Meissner, D. L., "Theoretical and Experimental Investigations of Fluid and Thermal Physics," M.S. Thesis, University of Toledo, Toledo, Ohio, 1992.
- [5] Bailey, A. B., "Flow Angle Measurements in a Rarefied Nozzle Plume," *AIAA Journal*, Vol. 25, No. 10, pp. 1303-1304, 1987.
- [6] Stephenson, W. B., "Use of the Pitot Tube in Very Low Density Flows," AEDC-TR-81-11, October 1981.
- [7] Legge, H., "Plume Impingement Forces on Inclined Flat Plates," *Proc. 17th International Symposium Rarefied Gas Dynamics*, VCH Verlag, Weinheim.
- [8] Lengrand, J. C., Allègre, J. and Raffin, M., "Underexpanded Free Jets and Their Interaction with Adjacent Surfaces," *AIAA Journal*, Vol. 14, pp. 692,694, 1976.
- [9] Penko, P. F., Boyd, I. D., Howell, T. G. and DeWitt, K. J., "Preliminary Experimental and Numerical Studies of Plume Impingement on a 100 Degree Cone," AIAA Paper 94-3142, 30th AIAA/ASME/SAE/ASEE Joint Propulsion Conference, Indianapolis, IN, June 1994.
- [10] Finke, R. C., Holmes, A. D. and Keller, T. A., "Space Environment Facility for Electric Propulsions Systems Research," NASA TN-D-2774, 1965.
- [11] Bird, G. A., *Molecular Gas Dynamics*, Clarendon Press, Oxford, 1976.
- [12] Kannenberg, K. C., Boyd, I. D. and Dietrich, S., "Development of an Object-Oriented Parallel DSMC Code for Plume Impingement Studies," AIAA Paper 95-2052, 30th AIAA Thermophysics Conference, San Diego, CA, June 1995.
- [13] Rothe, D. E., "Electron Beam Studies of Viscous Flow in Supersonic Nozzles," *AIAA Journal*, Vol. 9, No. 5, pp. 804-810, 1971.
- [14] Boyd, I. D., Penko, P. F., Meissner, D. L. and DeWitt, K. J., "Experimental and Numerical Investigations of Low-Density Nozzle and Plume Flows of Nitrogen," *AIAA Journal*, Vol. 30, No. 10, pp. 2453-2461, 1992.